Constraining Mass-Diameter Relations from Hydrometeor Images and Cloud Radar Reflectivities in Tropical Continental and Oceanic Convective Anvils

E. Fontaine[1], A. Schwarzenboeck[1], J. Delanoë[2], W. Wobrock[1], D. Leroy[1], R. Dupuy[1], C. Gourbeyre[1], A. Protat[2,*]

[1]{Université Blaise Pascal, Laboratoire de Météorologie Physique, Aubière, France}

[2]{Laboratoire Atmosphère, Milieux et Observations Spatiales, UVSQ, Guyancourt, France}

[*]{now at: Center for Australian Weather and Climate Research, Melbourne, Australia}

Correspondence to: E. Fontaine (E.fontaine@opgc.univ-bpclermont.fr)

Abstract

In this study the density of ice hydrometeors in tropical clouds is derived from a combined analysis of particle images from 2D-array probes and associated reflectivities measured with a Doppler cloud radar on the same research aircraft. Usually, the mass-diameter m(D) relationship is formulated as a power law with two unknown coefficients (pre-factor, exponent) that need to be constrained from complementary information on hydrometeors, where absolute ice density measurement methods do not apply. Here, at first an extended theoretical study of numerous hydrometeor shapes simulated in 3D and arbitrarily projected on a 2D plan allowed to constrain the exponent β of the m(D) relationship from the exponent σ of the surface-diameter S(D) relationship, which is likewise written as a power law. Since S(D) always can be determined for real data from 2D optical array probes or other particle imagers, the evolution of the m(D) exponent can be calculated. After that, the pre-factor α of m(D) is constrained from theoretical simulations of the radar reflectivities matching the measured reflectivities along the aircraft trajectory.

The study has been performed as part of the Megha-Tropiques satellite project, where two types of mesoscale convective systems (MCS) have been investigated: (i) above the African Continent and (ii) above the Indian Ocean. For the two datasets, two parametrisations are

derived to calculate the vertical variability of m(D) coefficients α and β as a function of the temperature. Originally calculated (with T-Matrix) and also subsequently parametrised m(D) relationships from this study are compared to other methods (from literature) of calculating m(D) in tropical convection. The significant benefit of using variable m(D) relations instead of a single m(D) relationship is demonstrated from the impact of all these m(D) relations on Z-CWC and Z-CWC-T fitted parametrisations.

1 Introduction

The French-Indian satellite Megha-Tropiques (MT), launched in 2011, is primarily devoted to improve our knowledge about the life cycle of tropical convective systems over ocean and continents, the environmental conditions for their formation and evolution, their water budget, and the associated water vapor transport. The most relevant instrument on the MT satellite for cloud studies is the MADRAS microwave imager having 9 frequencies (18.7 GHz to 157 GHz). Similar satellite missions for tropical cloud studies were TRMM (Tropical Rainfall Measurement Mission, Huffman et al. 2007; Jensen and Del Genio 2003) or SSM/I (Special Sensor Microwave/Imager, Spencer et al. 1989). To retrieve the surface rain rate from the brightness temperatures measured by above satellite missions, retrieval algorithms, as for example BRAIN (Viltard et al. 2006), are used, which have major sources of uncertainty due to the variability of the density of ice crystals in the tropical atmosphere.

With the overall objective to learn more about the variability of microphysical properties (in particular density) of ice crystals in tropical convective clouds, two aircraft campaigns (detailed in section 2) were conducted within the frame of the MT project.

The main focus of this study is to characterize the statistical relationship between the mass and the length (hereafter m(D)) of ice crystals by developing a retrieval technique that combines radar reflectivity and particle imagery, in order to produce reliable calculations of the condensed water content (CWC) as a function of time and along flight trajectory. This study focuses on the variability of the m(D) power law relationship in tropical convective clouds. Several previous studies have shown significant variability in m(D) including pre-factor and exponent of the power law for different flights within one and the same aircraft campaign (McFarquhar et al. 2007; Heymsfield et al. 2010a, hereafter denoted H10).

Concerning the ice crystal growth by pure vapor diffusion it is well known that the crystal habit is primarily a function of temperature and supersaturation (Bailey and Hallett 2004, 2009; Kobayashi 1993). In addition, collision growth processes (aggregation and riming) in dynamically more active clouds tremendously complicate the resulting crystal habits and associated properties (crystal geometry, density, optical properties). Therefore, and to improve our understanding of microphysical processes in clouds in general, it is necessary to get a more realistic description of ice crystals and particularly a description of their mass as a function of their size (Schmitt and Heymsfield 2010; hereafter SH2010).

Cloud observations are often related to radar measurements or satellite observations and associated inversion algorithms. Thus, the forward modeling of the remote sensing signal (active or passive) and the retrieval of cloud microphysics is linked to the model capacity to simulate the radiative transfer through a population of ice crystals of complex habits. Numerous previous studies already related cloud radar reflectivity (usually at a frequency of 94GHz or 35GHz) and in-situ measurements of cloud microphysical properties. For instance, Protat et al. (2007) and Hogan et al. (2006) calculated the total water content assuming a constant mass-size relationship for all clouds. Derived Z-CWC relationships often need to be corrected as a function of temperature. This somewhat translates the lack of knowledge of the temperature dependency of mass size relationships.

The most usual empirical expression used to predict the mass for various types of ice crystal shapes is formulated as a power law (Locatelli and Hobbs 1974; Mitchell 1996, hereafter M96; Heymsfield and Westbrook 2010; McFarquhar et al. 2007) which is usually a function of the maximum length (hereafter D_{max}) or the mean diameter (average of the maximum length in the y axis and the maximum value of x axis; Brown and Francis 1995, hereafter BF95) of the 2D hydrometeor images.

In this paper the mass m (in gram) is presented as a power law relation of D_{max} (in centimeters):

$$m(D_{\max}) = \alpha \cdot D_{\max}^{\beta} \quad (1)$$

In other studies the mass (and thus density) of hydrometeors has been determined following various principles. For example, ice crystals have been collected on a sheet of plastic or a Petri dish. After taking microphotographs of the crystals, these have been melted to deduce their mass from the resulting hemispherical drops (Locatelli and Hobbs 1974 ; Mitchell et al.

1990). Another method used is to classify hydrometeors according to their crystal habits associated to specific m(D) relations for individual habits, following the scheme given by Magono and Lee (1966). Furthermore, when the CWC mass concentration is measured directly with simultaneously 2D images of hydrometeors, m(D) relationships are derived from integral CWC data and corresponding particle size distributions (hereafter PSD) extracted from the images. BF95 used simultaneously a Lyman-α absorption hygrometer (Nicholls et al. 1990) and a 2D Optical Array Probe (OAP) to determine coefficients α and β for cirrus clouds. Heymsfield et al. (2002) developed an expression of the crystal mass as a function of D_{max} and the area ratio A_r (the projected area of an ice particle normalized by the area of a disc having the same D_{max}) for bullet-rosettes present in cirrus clouds. This approach was confronted with real measurements of CWC measured with a Counterflow Virtual Impactor (Ogren et al. 1985) and corresponding 2D images (OAP 2DC and 2DP) in cirrus clouds from airborne measurements. A detailed description of the particle habits which is needed for the previous approach was provided by the high resolution 2D images from the Cloud Particle Imager CPI (Lawson et al., 1998). Heymsfield et al. 2002 then used the retrieved m(D) relationships to compute Ka-band radar equivalent reflectivities, which are in good agreement with measured reflectivities.

Baker and Lawson (2006; hereafter B&L) introduced a new scheme which is a combination of fundamentals geometric parameters (perimeter, width, D_{max} and projected area) of the 2D images to deduce the mass of individual particles. This method was validated against the dataset of Mitchell et al. (1990) and has the advantage of not requiring particle habit assumptions.

McFarquhar et al. (2007) derived vertical profiles of m(D) relationships in the stratiform part of Mesoscale Convective Systems (hereafter MCS) above the North American continent within and below the melting layer. α and β coefficients were calculated from measured reflectivities and PSD deduced from the OAP 2DC and 2DP probes.

Schmitt and Heymsfield (2010, hereafter SH2010) have simulated the aggregation of plates or columns. Therein, fractal 2D and 3D analyses, calculated from the box counting method (Tang and Marangoni 2006), suggested that the fractal coefficient in the 3D space is equal to β. This allowed deriving a relationship that calculates the exponent β from the 2D fractal dimension of the 2D images. Once β has been fixed, the pre-factor α is calculated from the area measurement with OAP of ice hydrometeors. H10 have calculated m(D) coefficients by

minimizing the differences with measured CWC for different airborne campaigns. They demonstrate that a strong relationship exists between α and β coefficients, which was mathematically demonstrated with a gamma distribution parametrizing the PSD. Furthermore, they argue that the BF95 relationship overestimates the prefactor α for stratiform clouds, whereas α is underestimated for convective clouds.

In our study, bulk CWC measurements were either not performed (MT2010) or of limited value for MT2011. A deep cone unattended version of the Nevzorov probe has been installed under the fuselage, showing some enrichment due to ice crystals bouncing from the aircraft skin. In addition, a relatively high offset led to probe saturation at roughly 1gm^{-3}.

In order to calculate CWC, cloud ice density of hydrometeors needs to be derived from joint analysis of the radar reflectivity measured by the 94 GHz cloud radar RASTA (Protat et al. 2009), and cloud particle images measured simultaneously with 2D array probes on the same aircraft. The α and β coefficients are constrained from particle imagery and from theoretical simulations of ice crystal images, combined with subsequent simulations of cloud reflectivities compared to measured ones. In the following section 2 the MT aircraft campaigns and corresponding in-situ microphysical measurements are described. The methodology to retrieve m(D) coefficients for CWC calculations from the variability of the hydrometeor images and corresponding radar reflectivity measurements is presented in section 3. Section 4 then presents results on the variability (every 5 seconds during flight) of calculated m(D) coefficients. Then the coefficients are parametrized (as a function of temperature, also mean value) and compared with existing m(D) relations. All these m(D) relations are applied to datasets of the two MT flight campaigns, thus calculating CWC, in order to study their impact on Z-CWC and Z-CWC-T parametrisations fitted to corresponding measured reflectivity data.

2   Cloud data from the Megha-Tropiques flight campaigns

Two airborne measurement campaigns have been conducted with the French Falcon 20 research aircraft from SAFIRE (Service des Avions Français Instrumentés pour la Recherche en Environnement). During the first campaign, The Falcon20 has been flown out from Niamey (Niger), in August 2010 (hereafter MT2010) during the monsoon season above the West African continent. The second campaign has been conducted above the Indian Ocean between November and December 2011 (hereafter MT2011) at Gan (Maldives).

While African continental MCS in the monsoon seasons are due to the convergence of wet colder air masses from the ocean with dry warmer air masses, the convection over the Indian Ocean is due to the buoyancy of wet air masses leading to weaker convection in our case. Further studies (Cetrone and Houze 2009; Frey et al. 2011) have discussed differences in the intensity of tropical convection between pure continental African MCS and more maritime MCS with some continental influence (for example South Asia for oceanic convection north of Australia). These studies conclude on deeper convective systems and strongest precipitation for African MCS as compared to oceanic convection. Then growth processes of hydrometeors in oceanic convection were to a non negligible extent due to vapor diffusion producing many dendrites and plates that have been observed. In contrast, for West-African MCS the hydrometeor growth is more influenced by riming and aggregation processes, thus leading to observations of abundant ice crystal aggregates and graupel-type particles.

A brief description of the research flights and sampled convective cloud systems selected for this study is presented in Tab. 1. Cloud systems observed during MT2010 were typically MCS, consisting of a convective and a trailing stratiform part (Houze 2004). Most of the flights were performed in the stratiform part of these MCS within the temperature range down to -35°C. During MT2011, two types of systems were observed: in the first part of the campaign two MCS systems were sampled, whereas in the second part the convection has been much less organized and only more isolated smaller systems have been encountered. In general, flights were performed in the anvil at various constant altitude levels as close as possible and parallel to the convective line for MT2010. For MT2011 flight pattern were performed downstream the convective cell, but not crossing the most active part.

The Falcon 20 has been equipped with active remote sensing and cloud microphysics in situ instrumentation. Next to the Doppler Cloud radar RASTA (Protat et al. 2009) in-situ measurements of microphysical properties were performed using a new generation of Optical Array Probes (OAP): the 2-D stereo probe (2D-S) from Stratton Park Engineering Company (SPEC) Inc. which allows to monitor 2D images in the size range 10-1280µm, and the Precipitation Imaging Probe (PIP) from droplet Measurement Technologies (DMT) which measures hydrometeors in the size range of 100-6400 µm.

Fig. 1 presents exemplary 2D images of ice crystals observed during the two campaigns. 2D images are presented as a function of altitude. On the left side of Fig. 1 hydrometeors are shown that have been observed in continental MCS, whereas on the right side hydrometeors

observed in oceanic MCS are presented. In the two first levels (-1°C and -5°C) hydrometeors are similar with one exception where at -5°C a dendrite shows up for MT2011. For others levels ice crystal shapes are in general different. Besides aggregates, significant amounts of individual large pristine ice crystals such as dendrites (typically due to water vapor diffusion only) could be observed for MT2011, whereas 2D images for MT2010 generally look more like aggregates (more or less rimed) and sometimes graupels.

In order to derive particle size distributions and aspect ratios from the 2D images, standard corrections of the OAP data have been performed. In particular, rejection of 2D images due to shattering (Field et al. 2006, Korolev and Isaac 2005, Field et al. 2003) and also rejection of splashes have been applied. The inter-arrival time based shattering analysis is performed continuously to packages of 2000 particles along the flight track and 2D image data are corrected accordingly as a function of time. Moreover, reconstruction of truncated images which are only partially recorded has been applied (Heymsfield and Parrish 1978). Finally, the pixel resolution (10 μm for the 2D-S, 100 μm for the PIP) is corrected for the true air speed (Baumgardner and Korolev 1997), in order to account for the fixed speed setting during data acquisition.

2D images recorded with 2D-S and PIP probes were processed using the software developed at LaMP (Laboratoire de Météorologie Physique) for CPI images (Lefèvre 2007) and improved for black and white 2D images in order to extract a large variety of geometrical parameters, such as maximum diameter D_{max}, width perpendicular to D_{max} direction, projected area (hereafter Sp), and perimeter. Then for each probe, the number particle size distribution (PSD) and the mean aspect ratio distribution (hereafter AsD) are calculated as a function of D_{max}. With these distributions we build composite distributions for PSD and AsD from both probes. The size range of these distributions spans from 50 to 6450 microns in D_{max}. Equations 2 and 3 describe the simple interpolation scheme used to build the composite number PSD, an analogue scheme is used to derive AsD composite distributions.

$$\sum_{D_{max}=50}^{D_{max}<6450} N(D_{max}) \cdot \Delta D_{max} = \sum_{D_{max}=50}^{D_{max}<450} N_{2DS}(D_{max}) \cdot \Delta D_{max} + C_1(D_{max}) \cdot \sum_{D_{max}=450}^{D_{max}<950} N_{2DS}(D_{max}) \cdot \Delta D_{max}$$
$$+ C_2(D_{max}) \cdot \sum_{D_{max}=450}^{D_{max}<950} N_{PIP}(D_{max}) \cdot \Delta D_{max} + \sum_{D_{max}=950}^{D_{max}<6450} N_{PIP}(D_{max}) \cdot \Delta D_{max} \qquad (2)$$

with $C_1(D_{max}) + C_2(D_{max}) = 1$; and $C_2(D_{max}) = (D_{max} - 450)/(950 - 450)$ (3)

These composite distributions are mainly composed of three parts. The first part, which comprises the size range of 50-450 microns, is made of pure 2D-S distributions (N_{2D-S}), whereas the third part between 950-6400 microns is purely taken from PIP (N_{PIP}) distributions. The intermediate second part is obtained by weighting the 2D-S and PIP distributions with a transfer function (equation 3) which increases the weight of the PIP and decreases the weight of the 2D-S data with increasing D_{max}. The bin resolution of the composite distributions is given by ΔD_{max} equal to 10 microns. Examples of PSD and AsD are presented in Fig. 2. Fig. 2a shows the PSD composite distribution and the individual PSDs of the individual probes. The AsD composite distribution is shown in Fig. 2b. It can be seen that the transfer function smoothes the transition from the 2D-S to the PIP. In the common size range [450μm; 950μm] the two probes 2D-S and PIP are in rather good agreement. The 2D-S is most reliable and performing well up to particle sizes of 500 μm, beyond the 2D-S starts to be slowly affected by the truncation of the particles. This is why 2D-S images are taken into account with decreasing weight in the common size range [450μm; 950μm]. In contrast, the PIP is rather reliable beyond 900 μm. Below 900 μm, the PIP particles are taken into account with increasing weight, in order to ensure the continuity of the composite PSD calculated from 2D-S and PIP probe images. PSD (also AsD) and RASTA reflectivities are synchronized and averaged over the same time step of 5 seconds (for better PSD statistics). RASTA reflectivities measured 300m below (nadir) and 300m above the aircraft (zenith) along the flight trajectory are linearly interpolated to estimate the radar reflectivity at flight level. The uncertainty of the radar reflectivity is about 2dBZ, which takes into account measurement uncertainties and an eventual calibration error. For the MT data set it has been calculated that the mean reflectivity difference between 300m above and below the plane is in the order of 3 dBZ, which means a reflectivity difference between flight level and 300m above or below of about 1.5dBZ. This is less than the calibration and measurement error. Furthermore, the uncertainty in the measured concentrations of hydrometeors is estimated by the probe suppliers to be 20 %. This uncertainty stems mainly from the calculations of the sampling volume.

3   Methodology of m(D) retrieval: Studying 2D and 3D aspects of hydrometeors

3.1   Simulations of artificial ice crystal shapes and associated S(D) and m(D)

Optical array probes (OAP) measure the shadow projection of randomly oriented 3D cloud particles on a 2D plan. Theoretical simulations of 3D crystals have been processed, and are described in more detail in appendix A. The corresponding 2D projections are based on the principle of randomly oriented 3D particles projected on a 2D plan. These 2D images are processed with the same algorithm used for real particle images in order to deduce particle projected area Sp and maximum diameter D_{max} of each random projection. Overall, 45 different kind of hydrometeors (or habits) have been simulated and tested. Fig. 3 shows some examples of arbitrarily oriented 3D crystals (stellar, columns, plates, capped-columns, rosettes, and aggregates of those) that have been projected onto a plan. For each habit type numerous simulations and orientations are performed, then the projected surface Sp is fitted as a function of D_{max} (the relation is denoted S(D) ; equation 4), and likewise the mass is fitted as a function of D_{max} (see equation 1).

$$S(D_{\max}) = \gamma.D_{\max}^{\sigma} \qquad (4)$$

We assume random orientation, where each orientation has the same probability, and therefore not consider any possible effect of predominant orientation of hydrometeors during sampling. Probes are mounted under the wings at a distance of approximatively 0.5m, in addition, the probe tips exceed the wing leading edge. Deviations in exponents σ and β are further discussed in Appendix A. We assume extreme orientations for different habits, and analyse uncertainties of S(D) and m(D) relationships due to possible orientation of ice crystals.

Relationships S(D) and m(D) for each type of habit are fitted with power laws (equation 4 and equation 1). The resulting exponents σ for S(D) and β for m(D) are shown in Fig. 4 and reported in Tab. 2. In order to compare with existing values of σ and β found in the literature, we have added the values given in M96. In addition, Tab. 2 summarizes the values and the associated symbols of each simulated particle habit. The linear relationship fitted for β related to σ for 45 simulated habits is presented in equation 5, which is valid for σ in the range [1.05 ; 2], yielding values for β in the range [1 ; 2.94].

1     $\beta_\sigma\left(\pm0.16\right)=1.93\cdot\sigma-1.02$ (5)

2   There is no evidence of such a fit, neither in literature, nor in theory. From the obtained

3   results one can notice that varying the linear ratio between H and L for plates (also valid for

4   slender stellars, solid stellars, and rosettes) does not impact significantly σ and β, whereas a

5   nonlinear ratio $H=\sqrt{L}$ has more impact on both exponents. The latter case produces results

6   closer to measurements presented by M96 (Tab. 2), with simulations from our study resulting

7   in σ =1.86 and β = 2.49 and M96 measurements resulting in σ = 1.85 (for D_{max}<100µm) and β

8   = 2.45, respectively. For $D_{max} > 100$ µm, results are not readily comparable with the M96

9   results as in their study random orientation is not assumed. Regarding columns, an increase of

10   the ratio H/L has more impact on σ and β. As stated for hexagonal plates, also for columns the

11   nonlinear ratio $L=\sqrt{H}$ brings the simulations closer to the M96 measurements, with σ = 1.48

12   and β = 1.78 for simulations (this study) and σ = 1.41 and β = 1.74 for the M96

13   measurements. Other habits from the M96 measurements are not comparable to our

14   simulations.

15   In view of the results produced by the 3D simulations, it seems that β (and also σ) does not

16   relate much to the sphericity of the crystal shape, but more to how a population of ice crystals

17   is growing in the 3D space (axis x, y, z) as a function of its evolution in direction of its

18   maximum length. The behavior of β the exponent for plates and stellars but also for rosettes

19   shows that, if the crystal height grows at the same speed as the length (which is a combination

20   of the growth on 2 axis), then β is close to 3. In contrast, if the growth in length is two times

21   larger than the height, then β is closer to 2.5. Finally, if the height remain constant while the

22   length is growing, then β gets close to 2.

23   **3.2   Surface-diameter relationships of natural hydrometeors**

24   This section focuses on the S(D) relationship (see equation 4) and also on the correlation

25   which exists between D_{max}, Sp, and the mass of hydrometeors. Since ice crystals have

26   complex and varied shapes, the description of their volume (or mass) and their projected area

27   Sp as a function of the particle diameter cannot be described unambiguously with constant σ

28   exponents (for S(D)) or β (for m(D)). In this study, S(D) power law relations are calculated

29   for 5-seconds steps and are synchronized with PSD and RASTA reflectivity. To calculate

30   S(D), we plot the mean Sp of the particles versus their D_{max} (Fig. 5) for the two probes. Sp are

31   averaged by bins in order to get S(D) independently of the ice crystals concentration. S(D)

10

1 relations then are fitted by a power law described by γ and σ, for both probes, respectively.

2 On a log-log scale, *ln(γ)* represents the y-axis intercept and σ the slope of the linear

3 relationship such that *log(S) = σ*ln(D)+ ln(γ)*. S(D) relationships for the 2D-S and PIP probes

4 are calculated using particles larger than 250µm and 950µm, respectively. As shown in Fig. 5

5 S-D relationships calculated for submillimetric (2D-S) and millimetric particles (PIP) can

6 deviate. One can suppose that when S(D) of 2D-S and PIP are different, this implies to use σ

7 deduced from the 2D-S images ($\sigma_{2D\text{-}S}$) to calculate the β exponent for sub millimetric particles

8 ($\beta_{2D\text{-}S}$) and σ deduced from the PIP images (σ_{PIP}) to calculate the β exponent for the super-

9 millimetric particles (β_{PIP}). Then CWC would be calculated as follows:

10
$$CWC = \sum_{D_{max}=55\mu m}^{D_{max}=Dc} N(D\max) \cdot \alpha_{2DS} \cdot D_{max}^{\beta_{2DS}} \cdot \Delta D\max + \sum_{D_{max}=Dc}^{D_{max}=6450} N(D\max) \cdot \alpha_{PIP} \cdot D_{max}^{\beta_{PIP}} \cdot \Delta D\max \qquad (6).$$

11 Having fixed $\beta_{2D\text{-}S}$ and β_{PIP} would still mean that when constraining the prefactor of the m(D)

12 relation one needs to solve one equation with two unknowns for the two probes: $\alpha_{2D\text{-}S}$ and

13 α_{PIP}.

14 Therefore, we introduce here a single σ exponent taking into account images from 2D-S and

15 PIP probes, in order to calculate the variability of the m(D) coefficients from the variability of

16 S(D) relationships.

17
$$\sigma = \frac{\sum_{D_{max}=250\mu m}^{950\mu m} N(D_{max}) \cdot S(D_{max})}{\sum_{D_{max}=250\mu m}^{6450\mu m} N(D_{max}) \cdot S(D_{max})} \cdot \sigma_{2DS} + \frac{\sum_{D_{max}=950\mu m}^{6450\mu m} N(D_{max}) \cdot S(D_{max})}{\sum_{D_{max}=250\mu m}^{6450\mu m} N(D_{max}) \cdot S(D_{max})} \cdot \sigma_{PIP} \qquad (7)$$

18 This particular σ of equation 7 is calculated by weighting the exponent σ of each probe ($\sigma_{2D\text{-}S}$,

19 σ_{PIP}) with the ratio of the surface of ice crystals contained in the size range of the individual

20 probe (size range where individual S(D) relationship is calculated) over the entire surface

21 within the total size range covered by both probes.

22 **3.3 Mass-diameter coefficients and CWC retrieval**

23 In order to better understand the importance of coefficients α and β in eq. 1 and their impact

24 on the retrieved CWC, reflectivity simulations at 94GHz have been performed and compared

25 with corresponding measured reflectivities along the flight trajectory. Simulations of radar

26 reflectivities are complex when considering non-spherical ice crystals. Hogan et al. 2011,

27 have used the Rayleigh-Gans approximation to simulate the reflectivity of ice hydrometeors

1   interpreted as oblate spheroids (at 10GHz and 94GHz). Therein a constant aspect ratio of 0.6

2   was assumed to describe the flatening of the spheroids. Applying the BF95 parametrisation to

3   calculate CWC, a good agreement has been achieved between simulated and measured

4   reflectivities.

5   In this study, backscatter properties of the hydrometeors have been simulated with the T-

6   matrix method (Mishchenko et al. 1996) for crystals and/or with Mie theory for spherical

7   particles. In order to model the scattering properties of the ice particles, these particles are

8   assumed to be oblate spheroids with a flattening that equals the mean aspect ratio $\overline{As}$ of the

9   hydrometeors with $D_{max} < 2mm$, which impact most the simulated reflectivity:

10      $$\overline{As} = \sum_{D_{max}=55\mu m}^{2000\mu m} Pi(D_{max}) \cdot As(D_{max}) \qquad (8),$$

11   where the $Pi(Dmax)$ ist he weighting function and is calculated as follows:

12      $$Pi(D\max) = \frac{N(D_{max}) \cdot D_{max}^3 \cdot \Delta D_{max}}{\sum_{D_{max}=55\mu m}^{2000\mu m} N(D_{max}) \cdot D_{max}^3 \cdot \Delta D_{max}} \qquad (9).$$

13      $N(D_{max})$ is the concentration of the hydrometeors and $As(D_{max})$ their aspect ratio, both

14   functions of D_{max} . $\overline{As}$ is calculated every 5 seconds as is done for the composite PSD, σ, and

15   radar reflectivity. Indeed at 94GHz the hydrometeors with $D_{max} > 2mm$ are not invisible, but

16   the increase of their backscattering cross section ($Qback$; Fig. 6) as a function of their size is

17   not sufficient taking into account the very small crystal concentrations beyond a few

18   millimeters. Thus, they do not impact the simulated reflectivity. Fig. 6 also shows the impact

19   of $\overline{As}$ on the effective reflectivity for 94 GHz, for $\overline{As}$ varying between 0.5 and 1. For $\overline{As} = 1$

20   particles are sperical and therefore the Mie solution of the Maxwell's equation can be used.

21   For diameters less than 600-900 µm simulated radar reflectivities agree well with those

22   calculated using the Rayleigh approximation. As it can be seen in this figure, the so-called

23   'Mie effects' appear only for larger diameters and decreasing aspect ratio $\overline{As}$. The $Pi(D_{max})$

24   weighting function impacts the mean aspect ratio $\overline{As}$ which will be subsequently used to

25   constrain the T-matrix simulations of the radar reflectivity. In $Pi(D_{max})$ the maximum length

26   of hydrometeors is taken at its third order, to take into account the impact of the hydrometeors

27   in the sampling volume. This choice is a compromise to accomplish for the lack of knowledge

28   to constrain the variability of Q_{back} for natural ice crystals and previous approximations using

1 the Mie solution to model Q_{back}. Instead of the third order of D_{max}, we could have chosen the

2 number concentration $N(D_{max})$ or $N(D_{max}) \cdot S(D_{max})$, both may overestimate the smallest ice

3 crystals, while $D_{max}{}^{6}$ (Rayleigh approximation) does not seem to be the best choice either in

4 this context.

5 In general, we consider hydrometeors as a homogeneous mixture of ice and/or air. In order to

6 identify cases where the mixed phase (ice and water) was present, signals of the Rosemount

7 Ice Detector (RICE) have been analyzed. The RICE probe is in fact a supercooled water

8 detector. Few and extremely short cases were identified where the RICE probe showed

9 supercooled water. Data containing possible supercooled water have been excluded from

10 m(D) calculations for ice.

11 The dielectric properties of ice particles are linked to the mass-diameter relationship

12 characterised by the fraction of ice f_{ice} (equation 10) in the hydrometeors. Equation 10

13 explains how the ice fraction of the solid hydrometeors are calculated, with $\rho_{ice} = 0.917$g cm^{-3}.

14 The ice fraction f_{ice} cannot exceed 1.

15 $$f_{ice} = \min\left(1 \ , \ \frac{\alpha \cdot D_{max}^{\beta}}{\frac{\pi}{6} \cdot \rho_{ice} \cdot D_{max}^{3}}\right) \qquad (10).$$

16 Once f_{ice} is determined the refractive index is calculated using the approximation of Maxwell

17 Garnet (1904). The mass of the spheroid does not depend on the aspect ratio $\overline{As}$, but the

18 backscattering properties do. By means of the T-matrix method the backscattering coefficient

19 of a particle is calculated assuming the particle volume as an oblate spheroid with a diameter

20 $D_{T\text{-}matrix}$:

21 $$D_{Tmatrix} = D_{max} \cdot \sqrt[3]{\frac{1}{As}} \qquad (11).$$

22 In order to calculate the 94 GHz radar reflectivity, the particle number distribution $N(D_{max})$,

23 the mean aspect ratio $\overline{As}$, the ice fraction f_{ice} of the hydrometeors, and the β and α coefficients

24 of the mass-diameter relation (eq. 1) must be known or assumed. Fig. 7 gives an outline of the

25 technique developed to retrieve the m(D) coefficients. After fixing β_{σ} from equation 5, then

26 the prefactor α_{σ} is determined by minimizing the difference between the simulated and

1 measured reflectivities. Then the corresponding *CWC* in g m^{-3} is calculated from the PSD and

2 the mass-diameter coefficients:

$$3 \quad CWC(\alpha_\sigma, \beta_\sigma) = 10^3 \cdot \sum_{D_{max}=50\mu m}^{D_{max}=6400\mu m} N(D_{max}) \cdot \alpha_\sigma D_{max}^{\beta_\sigma} \cdot \Delta D_{max} \qquad (12).$$

4 Fig. 8 shows the temporal evolution of the PSD, mean aspect ratio $\overline{As}$, exponent β_σ, derived

5 α_σ, and calculated *CWC(α_σ, β_σ)* for a cloud sequence of flight 18 during MT2010. The

6 temporal variabilities of the PSD, $\overline{As}$, the exponent β_σ, constrained pre-factor α_σ, and *CWC*

7 are considerable.

8 The uncertainty of this method is evaluated in systematically varying β in the interval [1;3],

9 while for each β the pre-factor α is deduced accordingly by minimizing the difference

10 between the simulated and measured reflectivities. Then the corresponding *CWC* values are

11 calculated. For a given time step of 5 seconds the calculated minimum and maximum values

12 of CWC (*CWC$_{min}$* and *CWC$_{max}$*, respectively) are used to estimate the maximum uncertainty

13 (*ΔCWC$_{max}$*) of the retrieved *CWC*. *ΔCWC$_{max}$* is defined as the maximum difference between

14 *CWC(α_σ, β_σ)* and the largest or smallest value of *CWC*. This maximum uncertainty can be also

15 calculated in terms of the relative error in percent:

$$16 \quad 100.\frac{\Delta CWC_{max}}{CWC(\alpha_\sigma, \beta_\sigma)} = 100.\frac{MAX(\ [|CWC_{min} - CWC(\alpha_\sigma,\beta_\sigma)| \ ; \ |CWC_{max} - CWC(\alpha_\sigma,\beta_\sigma)|]\ )}{CWC(\alpha_\sigma, \beta_\sigma)} \quad (13).$$

17 For both measurement campaigns MT2010 and MT2011, Fig. 9 shows the distribution of

18 *ΔCWC$_{max}$* in percent. For most of the calculated *CWC* values the maximum errors remain

19 below 30%. Average values of the maximum deviations in *CWC* are 26% for MT2010 and

20 25% for MT2011, respectively.

21 *CWC(α_σ, β_σ)* is compared with the B&L scheme computing *CWC$_{B\&L}$* from the 2D images.

22 This method was chosen among others because it does not require any assumption on particle

23 habit and calculates the condensed mass particle by particle. Fig. 10 shows calculated

24 *CWC(α_σ, β_σ)* versus *CWC$_{B\&L}$*. The two CWC estimates are fitted using a power law. The

25 exponent found is close to 1 which indicates that we are close to linearity between the two

26 calculations for the two campaigns: 1.03 for MT2010 (Fig. 10a) and 1.01 for MT2011 (Fig.

27 10b). For MT2010 *CWC(α_σ, β_σ)* is 14% larger than *CWC$_{B\&L}$*, whereas for MT2011 *CWC(α_σ,*

28 *β_σ)* are close to *CWC$_{B\&L}$*. The data set of hydrometeors establishing the above B&L scheme

29 stems from winter storms in the central Sierra Nevada in the western part of the North

14

american continent. The crystals have been collected at the ground, and subsequently fitted to build the B&L scheme. The B&L scheme seems more appropriated to the MT2011 dataset than the MT2010 dataset. Comparisons between the two CWC retrieval methods also exhibit good correlation coefficients of 0.89 for MT2010 and 0.91 for MT2011, respectively. In addition, error bars for all analyzed CWC are given in Fig. 10 representing their minimum and maximum values which were determined using equation 13.

3.4 Impact of measurement uncertainties on m(D) and CWC retrieval

This section quantifies the impact of the measurement uncertainties in radar reflectivity, $\overline{As}$, β, PSD and also the probe shattering effect on the calculation of α and *CWC*. In order to quantify the impact of various measurement errors, the retrieval of α and subsequent calculation of *CWC* were performed in shifting measured values by the amount of the respective measurement error.

First, if reflectivity measured with the radar RASTA is shifted by +2 dBZ, then *CWC* increases by about 21% (Table 3). Second, if the mean aspect ratio $\overline{As}$ increases by 20% (due to a different calculation of the weighting function *Pi,* for example as a function of $N(D_{max})$), then CWC increases by about 12% (Table 4). Likewise, if *Pi(Dmax)* is calculated from $N(D_{max})*S(D_{max})$, then $\overline{As}$ increases by about 10% and *CWC* by about 6%. Third, a decrease in β_σ of -0.16, leads to a decrease in α_σ of about 28% on average, whereas an increase in β_σ of +0.16 increases the value of α_σ by about 42% on average. Fourth, in order to quantify the impact of particle shattering, α and *CWC* were calculated once without applying the removal algorithm. In this case the $S(D_{max})$ relationship is little impacted on average and the exponent β_σ of $m(D_{max})$ increases slightly by approximately +0.5%. The retrieved prefactor α_σ is impacted by about +4% and *CWC* increases by about +5%.

With respect to the concentration uncertainty ΔN when assuming an uncertainty in sampling volume of roughly 20% (uncertainty equally distributed over all sizes) we can estimate an uncertainty of 20% in α_σ. While the reflectivity is not impacted by the measurement uncertainty on the PSD, the CWC which corresponds to this reflectivity is not impacted to. Then, the CWC calculation from two concentrations N_1 and N_2 which gives the same CWC can be expressed as it follows:

$$CWC = \int_0^\infty N_1(D) \cdot \alpha_1 \cdot D^\beta \cdot dD = \int_0^\infty N_2(D) \cdot \alpha_2 \cdot D^\beta \cdot dD \quad (14)$$

Furthermore, assuming that β here is not impacted because the concentration uncertainty is assumed to be equally distributed over all diameters, then with $N_1(D) = (1 \pm \frac{\Delta N}{N}) \cdot N_2(D)$ we can derive $\alpha_1 = (1 \mp \frac{\Delta N}{N}) \cdot \alpha_2$, from where we conclude on an uncertainty for α_σ and CWC of roughly 20 %. The concentration uncertainties associated to the shattering are nevertheless mainly impacting the smaller sizes, the uncertainty of α_σ and CWC is then considered significantly smaller.

PSD used in this study solely take into account hydrometeors of D_{max} larger than 50µm, even though the 2D-S starts recording particles at 10µm. However, due to significant measurement uncertainties (shattering effects, out of focus particle sizes and related sampling volume) of the concentration of small particles of only a few pixels in size the composite PSD used and presented in this study do not take into account particle diameters below 50µm. The impact on CWC of 10-50µm size particles (not taken into account in this study) has been estimated, comparing CWC values calculated in parallel for PSD starting at 10 µm and starting at 50 µm. These comparisons illustrate that for more than 95% of the overall dataset, the small hydrometeors with diameters below 50µm would have increased CWC values presented in this study by less than 1%.

4   m(D) relationship and impact on Z-CWC calculation

4.1   m(D) variability

In the previous section, it has been demonstrated how β_σ is derived from $S(D_{max})$ power laws that are fitted separately for 2D-S and PIP image data with final calculation of one single exponent σ, yielding then β_σ based on the theoretical work presented in section 3.1. Then α_σ is constrained by reflectivies of RASTA, including subsequent calculation of CWC.

The two m(D) coefficients (α_σ, β_σ) appear to be strongly correlated with each other, with a correlation coefficient (cc) that equals 0.81 for MT2010 (Fig. 11a) and 0.92 for MT2011 (Fig. 11b). This result was observed and discussed in H10. In H10, m(D) coefficients were found by minimizing the differences between CWC estimated from particle imagery and measured

1 bulk CWC. This was performed flight-by-flight for different airborne campaigns. Their

2 dataset was divided into two types of cirrus: convective cirrus and stratiform cirrus. H10

3 obtained trends for each type of cirrus by fitting the mean of the prefactor (here α) as a

4 function of the exponent (here β). In Fig. 11, the power law fit obtained for convective cirrus

5 by H10 is added as a black line. We note in the semi-log representations of Fig. 11, that the

6 slope derived by H10 is exceeding the slopes calculated for MT2010 and MT2011,

7 respectively. This may be explained by the fact that β coefficients in H10 have been

8 calculated differently as compared to this study. However, both studies show that α (hereafter

9 α_β) can be fitted as an exponential function of β (equations 15 and 16 for MT2010 and

10 MT2011, respectively).

11 $MT2010:$ $\alpha_\beta = 7.10^{-5} \cdot e^{2.11 \cdot \beta_\sigma}$ (15)

12 $MT2011:$ $\alpha_\beta = 2.10^{-5} \cdot e^{2.65 \cdot \beta_\sigma}$ (16)

13 Furthermore, Fig. 11 reveals that temperature has an impact on the relationship between α_σ

14 and β_σ, which was not discussed in H10. In particular, for a given exponent β_σ, the prefactor

15 α_σ increases with temperature. Equations 17 and 18 take into account the temperature

16 dependency of the α-β relation, where the temperature is given in K and the resulting

17 prefactor is denoted $\alpha_{\beta,T}$.

18 $MT2010:$ $\alpha_{\beta,T} = 7.10^{-5} \cdot e^{2.11 \cdot \beta_\sigma} \cdot \left(0.05888 \cdot e^{0.0107 \cdot T} + 6.4.10^{-17} \cdot e^{0.133 \cdot T} \right)$ (17),

19 $MT2011:$ $\alpha_{\beta,T} = 2.10^{-5} \cdot e^{2.65 \cdot \beta_\sigma} \cdot 0.011834 \cdot e^{0.01535 \cdot T}$ (18).

20 Table 5 shows ratios of α_β and $\alpha_{\beta,T}$ (calculated according to equations 15, 16, 17, and 18) over

21 α_σ (constrained by T-matrix simulations). Average and median values of these ratios are

22 particularly close to 1. The first and third quartiles illustrate the narrowing around the median

23 ratio when parametrizing the α as a function of β and the temperature for the two campaigns.

24 For the two MT campaigns the following mean coefficients of m(D) have been deduced:

25 $MT2010:$ $m(D_{max}) = 0.0090 \cdot D_{max}^{2.23}$ (19),

26 $MT2011:$ $m(D_{max}) = 0.0054 \cdot D_{max}^{2.05}$ (20).

27 In Fig. 12 these relationships are compared against m(D) deduced in H10 on the hand for the

28 NAMMA (NASA African Monsoon Multidisciplinary Analyses; Zipser et al. 2009) campaign

1 and on the other hand for clouds which were convectively generated (hereafter cv-gt) during

2 CRYSTAL-FACE (Cirrus Regional Study of Tropical Anvils and Cirrus Layers–Florida Area

3 Cirrus Experiment ; Jensen et al. 2004) and TC4 (Tropical Composition, Cloud and Climate

4 Coupling ; Toon et al. 2010; Heymsfield et al. 2010b). NAMMA was performed above the

5 African continent. CRYSTAL-FACE took place in the southern part of Florida, whereas TC4

6 includes convective systems close to the Inter-Tropical Convergence Zone (ITCZ) and other

7 strong convection developed along the coast of Costa Rica. H10 fixed m(D) coefficients for

8 NAMMA such that $\alpha = 0.011$ and $\beta = 2.1$ and for cv-gt (CRYSTAL-FACE+TC4) $\alpha = 0.0063$

9 and $\beta = 2.1$. Furthermore, m(D) findings from M96 are also included in that figure. m(D)

10 relations of MT2011 and H10 for clouds convetively generated are very similar. The mean

11 m(D) derived for MT2010 yields crystal masses that are a factor of two smaller than those

12 given by H10 for NAMMA. Still, mean m(D) derived for MT2010, MT2011 and H10(cv-gt)

13 reveal higher masses than those given by M96 (for different crystal species) with the

14 exception for the lump graupel. The fact that H10 (NAMMA) found largest mass for ice

15 hydrometeors below 1mm in size may suppose that ice crystals were more rimed particles in

16 the vicinity of the convective part of MCS (NAMMA campaign) as compared to their

17 stratiform part (MT2010).

18 Fig. 13 presents trends of m(D) coefficients α_σ and β_σ with cloud altitude in terms of

19 temperature. The variability of m(D) coefficient at a given temperature is important. Average

20 m(D) coefficients (large stars in figure 13) have been calculated for temperature intervals of 5

21 K (in Fig. 13 large stars represent median values for respectice 5K temperature intervals). The

22 calculated profiles for MT2011data include solely flights 45 and 46 with a well developed

23 stratiform region of an extended convective system. Mean values of α_σ and β_σ are not

24 calculated beyond 272.5K temperature level, since the T-Matrix retrieval method does not

25 take into account the liquid water at the surface of melting ice crystals. This should have an

26 effect of increased reflectivity of ice crystals, leading to an underestimation of m(D)

27 coefficients. On average, mean β_σ coefficients (Fig. 13a) are larger for MT2010 than for

28 MT2011, whereas mean α_σ coefficients (Fig. 13b) are more similar and in the same order

29 between the level 260K-245K. The mean profiles show a decrease of mean α_σ and β_σ

30 coefficients with decreasing temperature described by equations 21 and 22:

31 $MT2010:$
$$\begin{cases} \alpha_T = 0.0020 \cdot e^{0.0037T} + 5.10^{-17} \cdot e^{0.1213T} \\ \beta_T = 7.13 \cdot e^{-0.0053T} + 5.4.10^{-7} \cdot e^{0.0435T} \end{cases} \quad (21)$$

1 *MT*2011:
$$\begin{cases} \alpha_T = 1.98.10^{-6} \cdot e^{0.0310T} \\ \beta_T = 1.81 \cdot e^{-0.000755T} - 1.027.10^7 \cdot e^{-0.07454T} \end{cases} \quad (22)$$

2 In addition, α and β profiles given by SH2010 for CRYSTAL-FACE and ARM (Atmospheric

3 Radiation Measurement) campaigns are added to figure 13. This latter dataset includes

4 midlatitude cirrus clouds generated from large scale uplift above the North American

5 continent. Globally, β_σ of MT2010 are similar to β of CRYSTAL-FACE, and β_σ of MT2011

6 are similar to β of ARM given in SH2010.

7 Table 6 shows ratios of α_T over α_σ and $CWC(\alpha_T, \beta_T)$ over $CWC(\alpha_\sigma, \beta_\sigma)$, as well as differencies

8 between β_T and β_σ. In general, α_σ for MT 2010 and MT2011 are overestimated by the fitted α_T,

9 whereas β_σ is underestimated for MT2010 and overestimated for MT2011 by the fitted β_T.

10 Finaly, the resulting *CWC* calculations lead to average ratios of $CWC(\alpha_T, \beta_T)/CWC(\alpha_\sigma, \beta_\sigma)$

11 $\approx$1.03 (median value $\approx$1.01) for MT2010 and $CWC(\alpha_T, \beta_T)/CWC(\alpha_\sigma, \beta_\sigma) \approx$0.94 (median value

12 ≈ 0.90) for MT2011.

13

14 **4.2   m(D) impact on Z-CWC and Z-CWC-T**

15 In the past, numerous studies have been dedicated to relating CWC to radar reflectivity (Liu

16 and Illingworth 2000; Hogan et al. 2006; Protat et al. 2007). These studies illustrate that CWC

17 can be estimated from the radar reflectivity at 94GHz or 35GHz using solely Z-CWC

18 relationships, but also when adding a temperature dependency (Z-CWC-T relationship). In the

19 following, $CWC(\alpha, \beta)$ has been calculated for MT2010 and MT2011 datasets according to 7

20 different methods: (1) T-matrix ($CWC(\alpha_\sigma, \beta_\sigma)$), (2) equations 17-18 ($CWC(\alpha_{\beta,T}, \beta_\sigma)$), (3)

21 equations 21-22 ($CWC(\alpha_T, \beta_T)$), (4) mean coefficients of equations 19-20 ($CWC(\alpha=0.0090,$

22 $\beta=2.23$ for MT2010*) and $CWC(\alpha=0.0054, \beta=2.05$ for MT2010)), (5) BF95 parametrisation,

23 (6) and (7) from H10 for NAMMA and cv-gt parametrisations, respectively. In order to use

24 the BF95 m(D) relationship, PSD were calculated for both MT campaigns such that the

25 particle diameter is $D = (Lx+Ly)/2$. H10 (NAMMA) parametrisation is used solely for the

26 MT2010 PSD data, whereas H10 (cv-gt) parametrisation is used for the MT2011 PSD data.

27 Table 7 gives an overview of Z-CWC and Z-CWC-T fitted relationships between different

28 $CWC(\alpha \beta)$ calculated with above methods and measured radar reflectivities (RASTA). The

29 fitted Z-CWC relations are presented in Fig. 14, whereas fitted Z-CWC-T relations are

30 presented in Fig. 15, with Z given in mm^6 m^{-3}, *CWC* in g m^{-3}, and T in K. In Fig. 14 and 15, Z

19

1   is expressed in dBZ for convenience. Two further relationships given by Protat and al. (2007),

2   hereafter denoted P2007 are added in Fig 14. Relationships given by P2007 are based on

3   cloud in-situ observations using a tropical dataset (equation 23a) and from a global dataset

4   (equation 23b) which includes also mid-latitude and tropical clouds. Note that the BF95 m(D)

5   relationship has been assumed for all clouds in P2007 calculations.

6    $CWC(Z) = 0.149 Z^{0.681}$ Global P2007 (23a)

7    $CWC(Z) = 0.198 Z^{0.701}$ Tropics P2007 (23b)

8   Applying P2007 parameterizations for calculating CWC results in significantly larger CWC

9   values, as compared to estimated CWC of this study for the Megha-Tropiques dataset, which

10   is particularly true for small reflectivities and most pronounced for MT2011 oceanic

11   convection. This might be due to the fact that the in-situ database used in P2007 encompasses

12   a much larger variety of ice clouds, including low CWC cirrus clouds.

13   For MT2010, largest CWC are found when CWC are calculated with the H10 parametrisation

14   for the NAMMA data. BF95 parametrisation calculates relatively low CWC values for all

15   reflectivities which is also the case for CWC calculated with the T-matrix method for

16   reflectivities below 0dBZ. The other parametrisations from this study and the P2007

17   parametrisation for the global dataset are similar and also close to T-matrix calculated CWC

18   in the range 5dBZ to 15 dBZ.

19   For MT2011, lowest CWC are calculated again with the BF95 parametrisation. CWC

20   calculations with H10 parametrisation for convectively generated clouds and most of the

21   parametrisations from this study are rather similar.

22   In general, for both campaigns CWC increases more significantly with the reflectivity when

23   calculated with the T-matrix method, as compared to CWC calculations from most m(D)

24   parametrisations (this study, H10, BF95).

25   In principal, Z-CWC-T relationships allow improving the calculation of more realistic CWC

26   as compared to simpler Z-CWC relationships. In table 8, for the two subsets of fitted

27   relationships (*CWC(Z)* and *CWC(Z, T)*), correlation coefficients (cc) are calculated between

28   *CWC(α, β)* and *CWC(Z)* or *CWC(Z, T)* fitted parametrisations, respectively. In addition, an

29   error calculation (equation 24) is performed with *error$_Z$* and *error$_{Z,T}$* defined as:

30   $error_Z = 100 \cdot \dfrac{|CWC(Z) - CWC(\alpha, \beta)|}{CWC(\alpha, \beta)}$ or $error_{Z,T} = 100 \cdot \dfrac{|CWC(Z,T) - CWC(\alpha, \beta)|}{CWC(\alpha, \beta)}$ (24).

1 Table 8 presents expected values (E), median values, first quartiles, third quartiles, and the

2 90th percentiles for $error_{Z,T}$ and $error_Z$, respectively. The lower part of this table presents the

3 calculation of $error_{Z,T}$ -$error_Z$ to demonstrate how CWC calculation from reflectivies is

4 improved when the temperature is parameterized in the fitted relationships between Z and

5 $CWC(\alpha, \beta)$.

6 Since the m(D) coefficients within this study have been constrained by the RASTA radar

7 reflectivity, it is not surprising that $error_Z$, $error_{Z,T}$, and also the difference between these two

8 errors ($error_{Z,T}$ -$error_Z$) are comparably small for CWC derived from T-Matrix method.

9 The fitted CWC-Z relationships for the other methods all produce significantly larger values

10 for $error_Z$ with maximum average $error_Z$ found for methods when $CWC(\alpha, \beta)$ has been

11 calculated from constant m(D) coefficients. Furthermore, $error_Z$ for all methods is generally

12 larger for MT2011 than for MT2010 dataset. When fitting CWC-Z-T, this does not improve

13 significantly correlations as compared to CWC-Z fitted relations, neither for the time resolved

14 T-matrix method nor for $CWC(\alpha_{T,\beta},\beta_\sigma)$ (equations 17 and 18) nor for $CWC(\alpha_T, \beta_T)$ (equations

15 21 and 22) methods, since therein the temperature has been implicitely taken into account for

16 $CWC(\alpha, \beta)$ calculation. In contrast, for the other methods applied to MT2010 and/or MT2011

17 datasets, as there are mean T-matrix, H10 (NAMMA), H10 (cv-gt), and BF95 the

18 improvement is significant when the temperature is taken into account. Moreover the

19 improvement is more efficient for these other methods for the MT2010 dataset ($error_Z$-

20 $error_{Z,T}$ improvement $>$ 10%) as compared to the MT2011 dataset ($error_Z$-$error_{Z,T}$

21 improvement $\leq$ 10%).

22 Without considering here the original T-Matrix method to calculate CWC, it can be clearly

23 seen from table 8 that the average $error_{Z,T}$ ($error_Z$, respectively) of all 6 remaining methods is

24 smaller for MT2010 $\approx$38% (40%) than for MT2011 $\approx$63% (71%).

25 The differencies in the performance of m(D) parametrisations and respective impact on

26 $CWC(Z)$ and $CWC(Z,T)$ relationships for MT2010 and MT2011 can be explained by the fact

27 that the mean aspect ratio $\overline{As}$ (Fig. 16) for MT2010 cloud particles shows rather constant

28 values with altitude including small standard deviations (Fig. 16a) and even a very small

29 standard deviation around the global average value (Fig. 16b). For MT2011 $\overline{As}$ shows a

30 broader distribution around the global average value and larger standard deviations with

31 altitude (Fig. 16c, 16a). On average $\overline{As}$ increases with altitude for MT2011, whereas $\overline{As}$ for

MT2010 remains more constant with altitude. Over 80% of the time $\overline{As}$ for MT2010 is in the range [0.55; 0.65] (Fig. 16b), whereas the broad $\overline{As}$ spectrum for MT2011 tends to larger values (up to 0.8), as compared to MT2010, which means that MT2011 contains significant amounts of particles with a more spherical aspect ratio.

5   Discussion and Conclusion

This study presents a method to calculate CWC from particle imagery and radar reflectivity at 94GHz. Cloud particles are represented by oblate spheroids used for reflectivity calculations with the T-matrix method. The flattening of the spheroid is constrained by the average aspect ratio $\overline{As}$ of the 2D images recorded by the 2D-S and the PIP probes. An estimation of the β exponent of the m(D) relationship is derived from the measurements of the projected surface of 2D images from 2D-S and PIP optical array probes. Then the prefactor α is calculated from simulated radar reflectivities matching the corresponding measured reflectivities at 94GHz. The method has been applied to two different datasets basically sampled in tropical stratiform anvils, the first one sampled over the African Continent (MT2010) and the second one collected over the Indian Ocean (MT2011).

An important variability of the m(D) coefficients has been found, especially for the MT2011 campaign. This result illustrates the main inconvenience to use a single m(D) relationships in tropical clouds. In this study two different parametrisations have been fitted to all constrained m(D) coefficients (5s time resolution) for continental (MT2010) and oceanic (MT2011) datasets in tropical convection. The first parametrisation allows us to calculate the m(D) prefactor as a function of the temperature and the m(D) exponent, showing that for a given exponent the prefactor increases with temperature for both campaigns. The second parametrisation allows us to deduce both m(D) coefficients (prefactor and exponent) as a function of the temperature. The latter result is in agreement with results shown in SH2010 for two different dataset of convective clouds in tropical and midlatitude conditions.

Furthermore, this study demonstrates how Z-CWC and Z-CWC-T relationships are impacted by different methods used to retrieve CWC from the measured PSD during MT2010 and MT2011. In general, the use of a single temperature independent m(D) relationship for all clouds is not appropriate, because it excludes the large natural variability of m(D) (as was also highlighted in Protat and Williams 2011).

1 For a series of different methods calculating $CWC(\alpha, \beta)$ (T-Matrix calculation and three

2 parametrisations presented in this study and also taken from literature such as H10 and BF95)

3 Z-CWC and Z-CWC-T relationships have been derived between $CWC(\alpha, \beta)$ and measured

4 radar reflectivities for MT2010 and MT2011 datasets. Subsequently, CWC derived from Z-

5 CWC and Z-CWC-T relations have been confronted with $CWC(\alpha, \beta)$ originally calculated

6 with the corresponding method.

7 The main result is shown with the improvement of decreasing error comparing Z-CWC-T

8 ($error_{Z,T}$) with Z-CWC fitted parametrisations ($error_Z$). For $CWC(\alpha, \beta)$ methods using

9 constant m(D) coefficients (mean T-Matrix, H10(NAMMA), H10(cv-gt), BF95) the error

10 improvement ($error_{Z,T}$ -$error_Z$) is significant, with on average -12% for MT2010 and –9% for

11 MT2011 datasets. In contrast, for $CWC(\alpha, \beta)$ methods which take into account the variability

12 of m(D) coefficients ($CWC(\alpha, \beta)$ as a function of temperature and more precisely as a function

13 of 2D images in original T-Matrix) the error improvement on average is merely -2% for

14 MT2010 and -4% for MT2011.

15 The fact that errors from Z-CWC-T (or Z-CWC) relations are larger for MT2011 than for

16 MT2010 dataset can be explained by the strong variability of the mean aspect ratio $\overline{As}$ of

17 cloud particles observed during MT2011, whereas cloud particles for MT2010 are showing a

18 narrower distribution of $\overline{As}$, meaning that crystals aspect ratios have been more uniform.

19 For MT2010 the parametrisation of m(D) coefficients with temperature (or altitude) seems to

20 perform well in order to describe the m(D) coefficients with on average $CWC(\alpha_T, \beta_T)/CWC(\alpha_\sigma,$

21 $\beta_\sigma) \approx 1.03$ and $CWC(\alpha_{\beta,T}, \beta_\sigma)/CWC(\alpha_\sigma, \beta_\sigma) \approx 1.08$. Likewise, values for MT2011 are

22 $CWC(\alpha_T, \beta_T)/CWC(\alpha_\sigma, \beta_\sigma) \approx 0.94$ and $CWC(\alpha_{\beta,T}, \beta_\sigma)/CWC(\alpha_\sigma, \beta_\sigma) \approx 0.99$ respectively. Despite

23 a good consistency for the both campaigns, the significant variability for example of α_T/α_σ, β_T-

24 β_σ, and $CWC(\alpha_T, \beta_T)/CWC(\alpha_\sigma, \beta_\sigma)$ has to be mentioned. The variability can be illustrated by 1st

25 and 3rd quartiles and is significantly higher for MT2011 than MT2010. This is due to the fact

26 that MT2011 dataset covers more variable microphysical properties and/or processes of

27 hydrometeors (significant contribution of water vapor diffusional growth) compared to

28 MT2010 and even temperature corrected parametrisations would need to be further refined.

29 An explanation could be that during MT2010 over the African continent the Falcon 20

30 research aircraft has been flying in stratiform parts of the MCS and despite the attempt to get

31 close to the convective cells, those have been too vigourous to be entered. Therefore the

32 microphysical properties of ice crystals in MCS systems sampled during MT2010 have been

1 relatively similar. In contrast, during MT2011 the less vigorous oceanic convection may have

2 been sampled partly during an earlier stage of convective activity and also crystal growth

3 regimes may have been different, leading to an increased variety of microphysical properties.

4

5 **APPENDIX A: Description of 3D simulations**

6 Simulations of 3D particle habits have been performed with the overall objective to study the

7 S(D) and m(D) relations including correlations between the two exponents of the power laws.

8 The simulated shapes aim to be realistic or at least comparable to the variety of hydrometeors

9 found in natural clouds. All crystal shapes considered have 3D characteristics with known

10 volume or mass and crystal orientations in the 3D space are fairly distributed. Zikmunda and

11 Vali 1972 show that rimed columns tends to be oriented in a way that the maximum length is

12 perpendicular to the fall velocity and rimed plates are oriented such that the maximum surface

13 is perpendicular to the motion. To quantify the uncertainty related to a possible predominant

14 crystal orientation during sampling, the crystal mass is calculated on the one hand from a

15 minimum D_{max} (which will be an underestimation with respect to its reel value) and on the

16 other hand from a maximum D_{max} (Fig. A1). By modeling both types of projected D_{max}

17 according to the crystal mass and doing this for all simulated shapes, we obtain the maximum

18 uncertainty related to the projection of possibly oriented 3D hydrometeors projected on a 2D

19 plane. On average it is found for all simulated habits that $\Delta\sigma= \pm0.15$ and $\Delta\beta= \pm0.31$.

20

21 **Plates**

22 The schematic of a plate type crystal is presented in Fig. A2. The geometric parameters used

23 are the thickness H and the height L between 2 opposed corners of the hexagon. The

24 simulations distinguish four types of plates, in order to explore the influence of the ratio

25 between H and L on the fitted power laws. Two simulations have a ratio of H/L equal to 0.1

26 and 0.2, whereas in the third simulation H is equal to the square root of L and in the fourth H

27 is constant and equal to 4 pixels. In all these simulations, L is chosen randomly out of the

28 interval from 20 to 200 pixels with 1000 thousands simulations of plates in each of the four

29 cases.

30 **Columns**

1 Fig. A3, shows the principal schematic of a column with geometric parameters of height H

2 and thickness L between 2 corners of the hexagon. As has been performed for the plates, four

3 sets of simulations were performed for columns: two with a linear ratio between H and L,

4 with H/L equal to 10 and 5, whereas in the third simulation L is equal to the square root of H

5 and in the fourth L is constant and equal to 16 pixels. H has been chosen out of the size range

6 of [10;100] pixels with 1000 simulations for columns in each of the four cases.

7 **Slender Stellars and more solid stellars**

8 Two types of stellar crystals were simulated with a significant difference in the width of their

9 branches (Fig. A4). We call these two types slender stellars (lower picture) and solid stellars

10 (upper picture). For both types of stellars, four sets of 1000 simulations were performed. Two

11 simulations have a ratio of H/L equal to 0.1 and 0.2, whereas in the third simulation H is equal

12 to the square root of L and in the fourth simulation H is constant and equal to 4 pixels.

13 **Capped Columns**

14 One type of capped columns was simulated and processed, where the column is capped by

15 two plates. The schematic description of a capped column is shown in Fig. A5. L_1 is the

16 height of the two plates (and large stellars) at the top of the column, L_2 ($=2.5L_1$) is the

17 thickness of the column, and H ($=L_1$) is its height. For the two simulations L_1 varied between

18 10 and 100 pixels and the width of the plates (or stellars) has been set to 4 pixels. In total

19 1000 simulations of capped columns were performed.

20 **Rosettes**

21 A rosette with six branches randomly oriented is shown in Fig. A6. To simplify the scheme of

22 the bullets that constitute the rosette, the bullets are assimilated as hexagonal columns. All the

23 bullets belonging to the same rosette have identical size parameters, where H is the bullet's

24 height, L its thickness, and N the maximum number of bullets building the rosette.

25 In total, eight series of simulations were performed, varying N between 3 and 6 bullets. Two

26 simulation series have been performed with N equal to 3 and where the bullets are described

27 either by L equal to the square root of H or L equal to 5 pixels. H has been chosen out of the

28 size range of 5 to 50 pixels.

29 Two sets of simulations followed where N is equal to 4 and where the bullets are described by

30 L equal to the square root of H or L equal to 10 pixels. H has been chosen out of the size

31 range of 10 to 100 pixels.

One set of simulations was performed where N is equal to 5 and where the bullets are described by the ratio *L/H* equal to 0.5. *H* has been chosen out of the size range of 10 to 100 pixels.

Finally, three additional sets of simulations were performed where *N* is equal to 6 and where the bullets are described either by *L* equal to the square root of *H* or by *L* equal to10 pixels or where the ratio *L/H* equal to 0.25. *H* has been chosen out of the size range of 10 to 100 pixels. All series were studied with 1000 simulations of rosettes.

Aggregates of individual crystal shapes

Furthermore, aggregates of the individual shapes presented above were also simulated. Without going into some details of crystal aggregation processes (Westbrook et al. 2004), here we solely study the phenomenon of 3D ice crystal aggregates projected on a 2D plane. The number of individual crystals (N_{agg}) used to form an aggregate has been varied. Individual crystals are randomly oriented in the 3D space, before they stick together forming the aggregate. An example of an aggregate of spheres is shown in Fig. A7. *N* is the random number of spheres, ranging between 3 and 50, which are aggregated, and *D* is the diameter of one sphere which is set constant and equals 6 pixels. In total 1000 simulations of aggregated spheres were performed.

APPENDIX B: List of Symbols

2D-S   2D stereographic optical array probe with a resolution of $10\mu m$ bin^{-1}

2D-C   2D cloud particle optical array probe with a resolution of $25\mu m$ bin^{-1}

2D-P   2D precipitation particle optical array probe with a resolution of $200\mu m$ bin^{-1}

α   pre-factor of mass-diameter relationship in general

α_β pre-factor of mass-diameter relationship calculated from the T-matrix method when β is calculated from equation 5

α_T pre-factor of mass-diameter relationship calculated as a function of the temperature (equations 21 and 22)

1	$\alpha_{\beta,T}$	pre-factor of mass-diameter relationship calculated as a function of the
2		temperature and β_σ (equations 17 and 18)
3	β	Exponent of mass-diameter relationship in general
4	β_T	Exponent of mass-diameter relationship calculated calculated in function of the
5		temperature (equations 21 and 22)
6	β_σ	Exponent of mass-diameter relationship calculated from equation 6
7	A_r	Area ratio: projected surface divided by $(\pi/4* D_{max}{}^2)$
8	As	Mean aspect ratio for a given D_{max} (=width/ D_{max})
9	AsD	Aspect ratio distribution
10	$\overline{As}$	Mean aspect ratio of all valid 2D images recorded during a 5s time period
11	BRAIN	Bayesian rain rate retrieval algorithm including neural network
12	CPI	Cloud particle imager, SPEC, Inc.
13	CWC	Condensed water content (in general)
14	$CWC_{B\&L}$	CWC deduced from the Baker and Lawson scheme
15	$CWC(\alpha_\sigma, \beta_\sigma)$	CWC calculated with α_σ and β_σ
16	$CWC(\alpha_T, \beta_T)$	CWC calculated with α_T and β_T
17	$CWC(\alpha_{\beta,T}, \beta_\sigma)$	CWC calculated with $\alpha_{\beta,T}$ and β_σ
18	D_{max}	Maximum length of the 2D images of the hydrometeors
19	ΔD_{max}	Bin resolution of the size distribution
20	$D_{T-matrix}$	Diameter of an oblate spheroid used by the T-matrix method
21	ΔCWC_{max}	Uncertainty of the retrieved CWC from RASTA reflectivity and 2D imagery of
22		OAP
23	$error_Z$	Absolute error using Z-CWC power fit and the retrieved CWC
24	$error_{Z,T}$	Absolute error using Z-CWC-T power fit and the retrieved CWC
25	f_{ice}	Ice fraction used fort the calculation of the backscattering properties of the
26	hydrometeors	

1	MADRAS	Microwave analysis & detection of rain & atmospheric systems
2	m(D)	Mass-diameter relationship
3	MT2010	Megha-Tropiques Falcon 20 measurement campaign (Niger, August 2010)
4 5	MT2011	Megha-Tropiques Falcon 20 measurement campaign (Gan, November-December 2011)
6	N_{2D-S}	Number concentration of hydrometeors counted by the 2D-S
7	N_{PIP}	Number concentration of hydrometeors counted by the PIP
8	N	Number concentration of hydrometeors
9	N_t	Total number concentration of hydrometeors
10	OAP	Optical array probe
11	Pi	Probability distribution function used to calculate the average aspect ratio
12	PIP	Precipitation Imaging Probe
13	PSD	Particle Size Distribution
14 15	RASTA	French acronym for Radar Aéroporté et Sol de Télédétection des propriétés nuAgeuse
16	ρ_{ice}	Ice density: 0.917 g cm^{-3}
17	S(D)	Surface-diameter relationship or area-diameter relationship
18	σ	Exponent of surface-diameter relationship in general
19	σ_{2D-S}	Exponent of surface-diameter relationship from the 2D-S 2Dimages
20	σ_{PIP}	Exponent of surface-diameter relationship from the PIP 2D images
21	Sp	Projected surface of a hydrometeor recorded by an OAP
22	T	Temperature in Kelvin
23	Q_{back}	Total backscattering coefficient as a function of D_{max} per bin
24	Z	RASTA reflectivity at 94GHz
25	Z-CWC	fitted power law between reflectivity and CWC

Z-CWC-T   fitted power law between reflectivity and CWC, adding a temperature dependency parametrisation

References

Bailey, M., and J. Hallett, 2004: Growth Rates and Habits of Ice Crystals between −20° and −70°C. *J. Atmospheric Sci.*, **61**, 514–544, doi:10.1175/1520-0469(2004)061<0514:GRAHOI>2.0.CO;2.

Bailey, M. P., and J. Hallett, 2009: A Comprehensive Habit Diagram for Atmospheric Ice Crystals: Confirmation from the Laboratory, AIRS II, and Other Field Studies. *J. Atmospheric Sci.*, **66**, 2888–2899, doi:10.1175/2009JAS2883.1.

Baker, B., and R. P. Lawson, 2006: Improvement in Determination of Ice Water Content from Two-Dimensional Particle Imagery. Part I: Image-to-Mass Relationships. *J. Appl. Meteorol. Climatol.*, **45**, 1282–1290, doi:10.1175/JAM2398.1.

Baumgardner, D., and A. Korolev, 1997: Airspeed Corrections for Optical Array Probe Sample Volumes. *J. Atmospheric Ocean. Technol.*, **14**, 1224–1229, doi:10.1175/1520-0426(1997)014<1224:ACFOAP>2.0.CO;2.

Brown, P. R. A., and P. N. Francis, 1995: Improved Measurements of the Ice Water Content in Cirrus Using a Total-Water Probe. *J. Atmospheric Ocean. Technol.*, **12**, 410–414, doi:10.1175/1520-0426(1995)012<0410:IMOTIW>2.0.CO;2.

Cetrone, J., and R. A. Houze, 2009: Anvil clouds of tropical mesoscale convective systems in monsoon regions. *Q. J. R. Meteorol. Soc.*, **135**, 305–317, doi:10.1002/qj.389.

Field, P. R., R. Wood, P. R. A. Brown, P. H. Kaye, E. Hirst, R. Greenaway, and J. A. Smith, 2003: Ice Particle Interarrival Times Measured with a Fast FSSP. *J. Atmospheric Ocean. Technol.*, **20**, 249–261, doi:10.1175/1520-0426(2003)020<0249:IPITMW>2.0.CO;2.

Field, A. J. Heymsfield, and A. Bansemer, 2006: Shattering and Particle Interarrival Times Measured by Optical Array Probes in Ice Clouds. *J. Atmospheric Ocean. Technol.*, **23**, 1357−1371, doi:10.1175/JTECH1922.1.

Frey, W., and Coauthors, 2011: In situ measurements of tropical cloud properties in the West African Monsoon: upper tropospheric ice clouds, Mesoscale Convective System

outflow, and subvisual cirrus. *Atmospheric Chem. Phys.*, **11**, 5569–5590, doi:10.5194/acp-11-5569-2011.

Heymsfield, A. J., and J. L. Parrish, 1978: A Computational Technique for Increasing the Effective Sampling Volume of the PMS Two-Dimensional Particle Size Spectrometer. *J. Appl. Meteorol.*, **17**, 1566–1572, doi:10.1175/1520-0450(1978)017<1566:ACTFIT>2.0.CO;2.

Heymsfield, A. J., and C. D. Westbrook, 2010: Advances in the Estimation of Ice Particle Fall Speeds Using Laboratory and Field Measurements. *J. Atmospheric Sci.*, **67**, 2469–2482, doi:10.1175/2010JAS3379.1.

Heymsfield, A. J., S. Lewis, A. Bansemer, J. Iaquinta, L. M. Miloshevich, M. Kajikawa, C. Twohy, and M. R. Poellot, 2002: A General Approach for Deriving the Properties of Cirrus and Stratiform Ice Cloud Particles. *J. Atmospheric Sci.*, **59**, 3–29, doi:10.1175/1520-0469(2002)059<0003:AGAFDT>2.0.CO;2.

Heymsfield, Z. Wang, and S. Matrosov, 2005: Improved Radar Ice Water Content Retrieval Algorithms Using Coincident Microphysical and Radar Measurements. *J. Appl. Meteorol.*, **44**, 1391–1412, doi:10.1175/JAM2282.1.

Heymsfield, C. Schmitt, A. Bansemer, and C. H. Twohy, 2010a: Improved Representation of Ice Particle Masses Based on Observations in Natural Clouds. *J. Atmospheric Sci.*, **67**, 3303–3318, doi:10.1175/2010JAS3507.1.

Heymsfield, G. M., L. Tian, A. J. Heymsfield, L. Li, and S. Guimond, 2010b: Characteristics of Deep Tropical and Subtropical Convection from Nadir-Viewing High-Altitude Airborne Doppler Radar. *J. Atmospheric Sci.*, **67**, 285–308, doi:10.1175/2009JAS3132.1.

Hogan, R. J., M. P. Mittermaier, and A. J. Illingworth, 2006: The Retrieval of Ice Water Content from Radar Reflectivity Factor and Temperature and Its Use in Evaluating a Mesoscale Model. *J. Appl. Meteorol. Climatol.*, **45**, 301–317, doi:10.1175/JAM2340.1.

Hogan, L. Tian, P. R. A. Brown, C. D. Westbrook, A. J. Heymsfield, and J. D. Eastment, 2011: Radar Scattering from Ice Aggregates Using the Horizontally Aligned Oblate Spheroid Approximation. *J. Appl. Meteorol. Climatol.*, **51**, 655–671, doi:10.1175/JAMC-D-11-074.1.

Houze, R. A., 2004: Mesoscale convective systems. *Rev. Geophys.*, **42**, n/a–n/a, doi:10.1029/2004RG000150.

Huffman, G. J., R. F. Adler, D. T. Bolvin, G. Gu, E. J. Nelkin, K. P. Bowman Y. Hong, E. F. Stocker, and D. B. Wolff, 2007: The TRMM Multisatellite Precipitation Analysis (TMPA): Quasi-Global, Multiyear, Combined-Sensor Precipitation Estimates at Fine Scales. *J. Hydrometeorol.*, **8**, 38–55, doi:10.1175/JHM560.1.

Jensen, E., D. Starr, and O. B. Toon, 2004: Mission investigates tropical cirrus clouds. *Eos Trans. Am. Geophys. Union*, **85**, 45–50, doi:10.1029/2004EO050002.

Jensen, M. P., and A. D. Del Genio, 2003: Radiative and Microphysical Characteristics of Deep Convective Systems in the Tropical Western Pacific. *J. Appl. Meteorol.*, **42**, 1234–1254, doi:10.1175/1520-0450(2003)042<1234:RAMCOD>2.0.CO;2.

Kobayashi, R., 1993: Modeling and numerical simulations of dendritic crystal growth. *Phys. Nonlinear Phenom.*, **63**, 410–423, doi:10.1016/0167-2789(93)90120-P.

Liu, C.-L., and A. J. Illingworth, 2000: Toward More Accurate Retrievals of Ice Water Content from Radar Measurements of Clouds. *J. Appl. Meteorol.*, **39**, 1130–1146, doi:10.1175/1520-0450(2000)039<1130:TMAROI>2.0.CO;2.

Locatelli, J. D., and P. V. Hobbs, 1974: Fall speeds and masses of solid precipitation particles. *J. Geophys. Res.*, **79**, 2185–2197, doi:10.1029/JC079i015p02185.

Maxwell Garnet, J. C., 1904: Colours in Metal Glasses and in Metallic Films. *Philos. Trans. R. Soc.*, 385–420, doi:10.1098/rsta.1904.0024.

McFarquhar, G. M., M. S. Timlin, R. M. Rauber, B. F. Jewett, J. A. Grim, and D. P. Jorgensen, 2007: Vertical Variability of Cloud Hydrometeors in the Stratiform Region of Mesoscale Convective Systems and Bow Echoes. *Mon. Weather Rev.*, **135**, 3405–3428, doi:10.1175/MWR3444.1.

Mishchenko, M. I., L. D. Travis, and D. W. Mackowski, 1996: T-matrix computations of light scattering by nonspherical particles: A review. *J. Quant. Spectrosc. Radiat. Transf.*, **55**, 535 – 575, doi:10.1016/0022-4073(96)00002-7.

Mitchell, D. L., 1996: Use of Mass- and Area-Dimensional Power Laws for Determining Precipitation Particle Terminal Velocities. *J Atmos Sci*, **53**, 1710–1723, doi:10.1175/1520-0469(1996)053<1710:UOMAAD>2.0.CO;2.

Mitchell, R. Zhang, and R. L. Pitter, 1990: Mass-Dimensional Relationships for Ice Particles and the Influence of Riming on Snowfall Rates. *J. Appl. Meteorol.*, **29**, 153–163, doi:10.1175/1520-0450(1990)029<0153:MDRFIP>2.0.CO;2.

Nicholls, S., J. Leighton, and R. Barker, 1990: A New Fast Response Instrument for Measuring Total Water Content from Aircraft. *J. Atmospheric Ocean. Technol.*, **7**, 706–718, doi:10.1175/1520-0426(1990)007<0706:ANFRIF>2.0.CO;2.

Ogren, J. A., J. Heintzenberg, and R. J. Charlson, 1985: In-situ sampling of clouds with a droplet to aerosol converter. *Geophys. Res. Lett.*, **12**, 121–124, doi:10.1029/GL012i003p00121.

Protat, A., and C. R. Williams, 2011: The Accuracy of Radar Estimates of Ice Terminal Fall Speed from Vertically Pointing Doppler Radar Measurements. *J. Appl. Meteorol. Climatol.*, **50**, 2120–2138, doi:10.1175/JAMC-D-10-05031.1.

Protat, A., J. Delanoë, D. Bouniol, A. J. Heymsfield, A. Bansemer, and P. Brown, 2007a: Evaluation of Ice Water Content Retrievals from Cloud Radar Reflectivity and Temperature Using a Large Airborne In Situ Microphysical Database. *J. Appl. Meteorol. Climatol.*, **46**, 557–572, doi:10.1175/JAM2488.1.

1 Protat, A., J. Delnoë, P. T. May, A. Plana-Fattori, A. Hasson, E. O'Connor, U. Görsdorf, and
2   A. J. Heymsfield, 2009: Assessment of Cloudsat Reflectivity Measurements and Ice
3   Cloud Properties Using Ground-Based and Airborne Cloud Radar Observations. *J.*
4   *Atmospheric Ocean. Technol.*, **26**, 1717–1741, doi:10.1175/2009JTECHA1246.1.

5 Schmitt, C. G., and A. J. Heymsfield, 2010a: The Dimensional Characteristics of Ice Crystal
6   Aggregates from Fractal Geometry. *J. Atmospheric Sci.*, **67**, 1605–1616,
7   doi:10.1175/2009JAS3187.1.

8 Spencer, R. W., H. M. Goodman, and R. E. Hood, 1989: Precipitation Retrieval over Land
9   and Ocean with the SSM/I: Identification and Characteristics of the Scattering Signal.
10   *J. Atmospheric Ocean. Technol.*, **6**, 254–273, doi:10.1175/1520-
11   0426(1989)006<0254:PROLAO>2.0.CO;2.

12 Tang, D., and A. G. Marangoni, 2006: 3D fractal dimension of fat crystal networks. *Chem.*
13   *Phys. Lett.*, **433**, 248 – 252, doi:http://dx.doi.org/10.1016/j.cplett.2006.11.057.

14 Toon, O. B., D.O. Star, E.J. Jensen, P.A. Newman, S. Platnick, M.R. Schoeberl, P.O.
15   Wennberg, S.C. Wofsy, M.J. Kurylo, H. Maring, K.W. Jucks, M.S. Craig, M.F.
16   Vasques, L. Pfister, K.H. Rosenlof, H.B. Selkirk, P.R. Colarco, S.R. Kawa, G.G.
17   Mace, P. Minnis and K.E. Pickering, 2010: Planning, implementation, and first results
18   of the Tropical Composition, Cloud and Climate Coupling Experiment (TC4). *J.*
19   *Geophys. Res. Atmospheres*, **115**, n/a–n/a, doi:10.1029/2009JD013073.

20 Viltard, N., C. Burlaud, and C. D. Kummerow, 2006: Rain Retrieval from TMI Brightness
21   Temperature Measurements Using a TRMM PR–Based Database. *J. Appl. Meteorol.*
22   *Climatol.*, **45**, 455–466, doi:10.1175/JAM2346.1.

23 Westbrook, C. D., R. C. Ball, P. R. Field, and A. J. Heymsfield, 2004: Theory of growth by
24   differential sedimentation, with application to snowflake formation. *Phys Rev E*, **70**,
25   021403, doi:10.1103/PhysRevE.70.021403.

26 Zikmunda, J., and G. Vali, 1972: Fall Patterns and Fall Velocities of Rimed Ice Crystals. *J.*
27   *Atmospheric Sci.*, **29**, 1334–1347, doi:10.1175/1520-
28   0469(1972)029<1334:FPAFVO>2.0.CO;2.

29 Zipser, E. J., C.H. Twohy, S-C. Tsay, N.C. Hsu, G.M. Heymsfield, K.L. Thornhill, S. Taneli,
30   R. Robert, T.N. Krishnamurti, Q. Ji, G. Jenkins, S. Ismail, R. Ferrare, G. Chen, E.V.
31   Browell, B. Anderson, R. Hood, H.M. Goodman, A.J. Heymsfield, J. Halverson, J.P.
32   Dunion, M. Douglas and R. Cifelli, 2009: The Saharan Air Layer and the Fate of
33   African Easterly Waves—NASA's AMMA Field Study of Tropical Cyclogenesis.
34   *Bull. Am. Meteorol. Soc.*, **90**, 1137–1156, doi:10.1175/2009BAMS2728.1.

35

36

1 TABLE 1. List of Falcon 20 research flights used in this study.

Flight program	Flight number	Day	Hour (UTC)	Cloud type
MT2010 Continental	Flight 15	2010/08/06	1610-1900	MCS squall line
	Flight 17	2010/08/10	0845-1160	MCS squall line
	Flight 18	2010/08/13	1320-1625	MCS squall line
	Flight 19	2010/08/17	1030-1340	MCS squall line
	Flight 20	2010/08/17	2335-0240	MCS squall line
MT2011 Oceanic	Flight 45	2011/11/27	0530-0850	MCS ITCZ
	Flight 46	2011/11/27	1515-1825	MCS ITCZ
	Flight 49	2011/12/06	1325-1540	Isolated Convective System
	Flight 50	2011/12/08	0600-0900	Isolated Convective System

2

3

1   TABLE 2. Ice crystal types and corresponding exponents σ and β of S(D) and m(D) relations.

2   The symbols in the left column are subsequently used in Fig. 4 for individual ice crystal

3   shapes. The first part of the table stems from Mitchell (1996) where random orientation is

4   assumed for particles with D_{max} < 100µm and horizontal orientation is assumed for particles

5   beyond 100 µm. The second part of the table stems from simulations.

symbol	Description	Range	σ	β
	Ice crystal shapes from Mitchell (1996)			
◆	hexagonal plates	15µm<D_{max}<100µm	1.85	2.45
◇	hexagonal plates	100<D_{max}<3000µm	2	2.45
■	hexagonal columns	30<D_{max}<100µm	2	2.91
■	hexagonal columns	100<D_{max}<300µm	1.5	1.91
■	hexagonal columns	D_{max}>300µm	1.41	1.74
■	rimed long columns	200<D_{max}<2400µm	1.41	1.8
★	crystals with sector-like branches(P1b)	10<D_{max}<40µm	1.85	2.42
★	crystals with sector-like branches(P1b)	40<D_{max}<2000µm	1.97	2.02
★	broad-branched crystals (Plc)	10<D_{max}<100µm	1.85	2.42
★	broad-branched crystals (Plc)	100<D_{max}<1000µm	1.76	1.8
★	stellar crystals with broad arms (P1d)	10<D_{max}<90µm	1.85	2.42
★	stellar crystals with broad arms (P1d)	90<D_{max}<1500µm	1.63	1.67
★	densely rimed dendrites (R2b)	1800<D_{max}<4000µm	1.76	2.3
◆	side planes (S1)	300<D_{max}<2500µm	1.88	2.3
✚	bullet rosettes, 5 branches at -42°C	200<D_{max}<1000µm	1.57	2.26
◀	aggregates of side planes	600<D_{max}<4100µm	1.88	2.2
◀	aggregates of side planes, columns & bullets (S3)	800<D_{max}<4500µm	1.88	2.1
▲	assemblies of planar poly-crystals in cirrus clouds	20<D_{max}<450µm	1.88	2.45
●	lump graupel (R4b)	500<D_{max}<3000µm	2	2.8
●	hail	5000<D_{max}<25000µm	2	3
	Simulations of Ice-Crystals shape			
■	columns (H=5*L)	100<D_{max}<1000µm	1.86	2.53
■	columns (H=10*L)	100<D_{max}<1000µm	1.87	2.44
■	columns (L=160µm)	100<D_{max}<1000µm	1.06	1.04
■	columns ($L=\sqrt{H}$)	100<D_{max}<1000µm	1.48	1.78
★	thick star (H = 0.2*L)	200<D_{max}<1200µm	1.98	2.89
★	thick star (H = 0.1*L)	200<D_{max}<1200µm	1.99	2.86
★	thick stars (H=40µm)	200<D_{max}<1200µm	1.49	2.06
★	thick stars ($H=\sqrt{L}$)	200<D_{max}<1200µm	1.76	2.48
★	thin Stars (H=0.2*L)	100<D_{max}<1000µm	1.96	2.89
★	thin Stars (H=0.1*L)	100<D_{max}<1000µm	1.94	2.75
★	Thin Stars (H=40µm)	100<D_{max}<1000µm	1.39	2.06
★	thin Stars ($H=\sqrt{L}$)	100<D_{max}<1000µm	1.74	2.51
◆	plates (H= 0.2*L)	200<D_{max}<2000µm	1.95	2.96
◆	plates (H = 0.1*L)	200<D_{max}<2000µm	1.92	2.91
◆	plates (H=40µm)	200<D_{max}<2000µm	1.65	2.03
◆	plates ($H=\sqrt{L}$)	200<D_{max}<2000µm	1.86	2.49
✖	Rosettes (L= 50µm ; Nmax=3)	50<D_{max}<500µm	1.37	1.04
✖	Rosettes ($L=\sqrt{H}$; Nmax=3)	50<D_{max}<500µm	1.69	2.21

	Description	D_{max} range		
	Rosettes (L=100μm ; Nmax=4)	$100<D_{max}<1000$μm	1.39	1.26
	Rosettes ($L=\sqrt{H}$; Nmax=4)	$100<D_{max}<1000$μm	1.65	2.16
	Rosettes (L=0.5H ; Nmax=5)	$500<D_{max}<2000$μm	1.83	2.9
	Rosettes (L=0.25H ; Nmax=6)	$500<D_{max}<2500$μm	1.78	2.97
	Rosettes(L=100μm ; Nmax=6)	$100<D_{max}<1000$μm	1.42	1.25
	Rosettes($L=\sqrt{H}$; Nmax=6)	$100<D_{max}<1000$μm	1.66	2.16
	Capped columns (2 thick stars: $L_2=2.5L_1$; H= L_1)	$150<D_{max}<1400$μm	1.79	2.21
	Capped columns (2 plates: $L_2=2.5L_1$; H= L_1)	$150<D_{max}<1400$μm	1.92	2.43
	$8<N_{agg}<30$ thick stars ($H=\sqrt{L}$) Individual Diameter such : $300 < L < 400$μm	$1000<D_{max}<4000$	1.79	1.92
	$8<N_{agg}<30$ plates (H = 0.1*L) Individual Diameter such : $200 < L < 300$μm	$600<D_{max}<2000$	1.8	1.81
	$8<N_{agg}<30$ plates ($H=\sqrt{L}$) Individual Diameter such : $200 < L < 300$μm	$600<D_{max}<2500$	1.59	1.69
	$2<N_{agg}<4$; columns (L=160μm) Individual Diameter such : $400 < H < 600$	$400<D_{max}<1500$	1.26	1.75
	$2<N_{agg}<4$; columns ($L=\sqrt{H}$) Individual Diameter such : $400 < H < 600$	$200<D_{max}<1000$	1.45	2.07
	$2<N_{agg}<4$; thick stars (H= 0.2*L) Individual Diameter such : $400 < L < 600$μm	$400<D_{max}<3000$	1.82	2.62
	$2<N_{agg}<4$; thick stars (H= 0.1*L) Individual Diameter such : $400 < L < 600$μm	$400<D_{max}<3000$	1.63	2.62
	$2<N_{agg}<4$; thick stars (H= 40μm) Individual Diameter such : $400 < L < 600$μm	$400<D_{max}<3000$	1.87	2.25
	$2<N_{agg}<4$; thick stars ($H=\sqrt{L}$) Individual Diameter such : $400 < L < 600$μm	$400<D_{max}<3000$	1.72	2.46
	$2<N_{agg}<4$; thin stars (H= 0.2*L) Individual Diameter such : $300 < L < 600$μm	$300<D_{max}<2000$	1.64	2.52
	$2<N_{agg}<4$; thin stars (H= 0.1*L) Individual Diameter such : $300 < L < 500$μm	$300<D_{max}<1500$	1.72	2.52
	$2<N_{agg}<4$; thin stars (H= 40μm) Individual Diameter such : $300 < L < 500$μm	$300<D_{max}<1500$	1.46	2.14
	$2<N_{agg}<4$; thin stars ($H=\sqrt{L}$) Individual Diameter such : $300 < L < 500$μm	$300<D_{max}<2000$	1.53	2.37
	$2<N_{agg}<4$; plates (H= 0.2*L) Individual Diameter such : $300 < L < 500$μm	$300<D_{max}<2000$	1.87	2.57
	$2<N_{agg}<4$; plates (H= 0.1*L) Individual Diameter such : $300 < L < 500$μm	$300<D_{max}<1500$	1.61	2.37
	$2<N_{agg}<4$; plates (H= 40μm) Individual Diameter such : $300 < L < 500$μm	$300<D_{max}<1500$	1.64	1.99
	$2<N_{agg}<4$; plates ($H=\sqrt{L}$) Individual Diameter such : $300 < L < 600$μm	$300<D_{max}<1500$	1.76	2.29
	$3 < N_{agg} < 20$; spheres Individual Diameter such : D = 60μm ;	$200<D_{max}<2000$μm	1.45	1.74
	$3 < N_{agg} < 50$; spheres Individual Diameter such : D = 150μm ;	$100<D_{max}<1000$μm	1.54	1.84

1

1 TABLE 3. Uncertainty of retrieved α and CWC as a function of the uncertainty of the measured

2 reflectivity.

ΔZ [dBZ]	Δα (%)	ΔCWC (%)
-2	-26	-26
-1	-12	-12
+1	+11	+11
+2	+21	+21

3

4 TABLE 4. Uncertainty of retrieved α and CWC as a function of the uncertainty of the average

5 aspect ratio of 2D images.

$\Delta \overline{As}$ (%)	Δα (%)	ΔCWC (%)
-20	-12	-12
-10	-6	-6
+10	+6	+6
+20	+13	+13

6

7 TABLE 5. Ratios of fitted α_β *and* $\alpha_{\beta,T}$ over retrieved α_σ from T-matrix calculations. Average

8 ratios are given in column E. Quartile, median, third quartile, are given in 1/4, 1/2 , and 3/4

9 columns.

	E	1/4	1/2	3/4
MT2010 : $\alpha_\beta/\alpha_\sigma$	1.07	0.66	1.03	1.47
MT2011 : $\alpha_\beta/\alpha_\sigma$	1.03	0.54	0.95	1.53
MT2010 : $\alpha_{\beta,T}/\alpha_\sigma$	1.08	0.91	1.03	1.20
MT2011 : $\alpha_{\beta,T}/\alpha_\sigma$	0.99	0.74	0.92	1.13

10

1 TABLE 6. Ratio of fitted α_T over retrieved α_σ, and of $CWC(\alpha_T, \beta_T)$ calculated from fitted α_T

2 and β_T over $CWC(\alpha_\sigma, \beta_\sigma)$ calculated with T-matrix retrieved α_σ and β_σ. In addition, differencies

3 between β_T and β_σ are shown. Expected values of ratios and differencies are given in column

4 E. first quartile, median, and third quartile are given in 1/4, 1/2, and 3/4 columns.

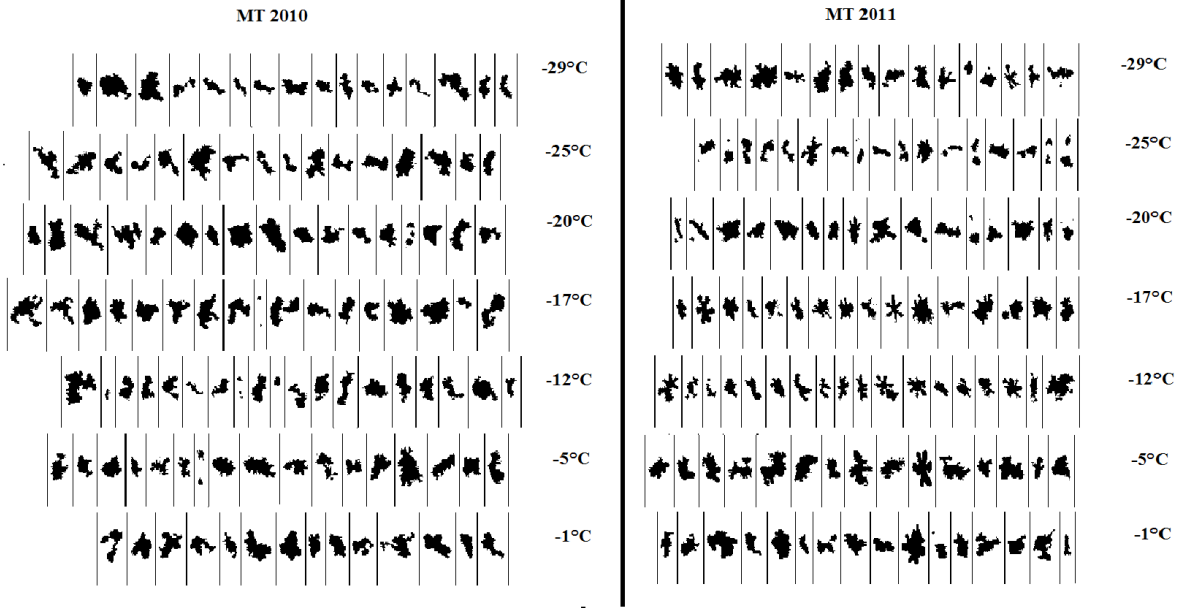|	E	1/4	1/2	3/4
MT2010 : α_T/α_σ	1.12	0.77	0.98	1.23
MT2010 : $\beta_T-\beta_\sigma$	-0.02	-0.14	-0.03	+0.08
MT2010: $CWC(\alpha_T,\beta_T)/CWC(\alpha_\sigma, \beta_\sigma)$	1.03	0.86	0.98	1.15
MT2011 : α_T/α_σ	1.35	0.61	1.01	1.60
MT2011 : $\beta_T-\beta_\sigma$	+0.03	-0.13	+0.03	+0.21
MT2011: $CWC(\alpha_T,\beta_T)/CWC(\alpha_\sigma, \beta_\sigma)$	0.94	0.70	0.90	1.09

5

6 TABLE 7. Fitted Z-CWC and Z-CWC-T relationships according to $CWC(\alpha, \beta)$ calculations

7 with different methods for MT2010 and MT2011 datasets.

|	CWC(Z)	CWC(Z, T)
T-matrix(MT2010)	$CWC=0.0981*Z^{0.805}$	$CWC = 0.7183*e^{-0.0078913*T} .Z^{(-0.002549*T+1.4813)}$
T-matrix (MT2011)	$CWC= 0.0869*Z^{0.775}$	$CWC = 18.4392*e^{-0.02115*T} .Z^{(0.002659*T+0.13467)}$
MT2010(equation17)	$CWC = 0.1421*Z^{0.655}$	$CWC = 0.44974*e^{-0.004527*T} .Z^{(-0.0044794*T+1.8224)}$
MT2011(equation18)	$CWC = 0.0893*Z^{0.682}$	$CWC = 0.93632*e^{-0.0093472*T} Z^{(-0.0017635T+1.1748)}$
mean(MT2010)(equation19)	$CWC = 0.1490*Z^{0.659}$	$CWC =62.9368*e^{-0.023757*T} .Z^{(-0.002388*T+1.3059)}$
mean(MT2011)(equation20)	$CWC = 0.1084*Z^{0.656}$	$CWC =65.3563*e^{-0.025176*T} .Z^{(-0.0019304*T+1.2195)}$
MT2010(equation21)	$CWC = 0.1261*Z^{0.686}$	$CWC = 0.3365*e^{-0.0037815*T} .Z^{(-0.0026268*T+1.3679)}$
MT2011(equation22)	$CWC = 0.0826*Z^{0.708}$	$CWC = 0.12055*e^{-0.0016174*T} .Z^{(-0.0021477*T+1.2853)}$
H10(NAMMA)	$CWC = 0.2397*Z^{0.664}$	$CWC = 446.6519*e^{-0.029602*T} .Z^{(-0.0012781*T+1.0319)}$
H10(cv-gt)	$CWC = 0.1101*Z^{0.662}$	$CWC = 52.153*e^{-0.024225*T} .Z^{(-0.0020589*T+1.2569)}$
BF95 (MT2010)	$CWC = 0.0797*Z^{0.668}$	$CWC = 856.8913*e^{-0.036509*T} .Z^{(-0.0001986*T+0.76656)}$.
BF95 (MT2011)	$CWC = 0.0694*Z^{0.635}$	$CWC = 112.1674*e^{-0.02908*T} .Z^{(-0.00076668*T+0.90401)}$

8

9 TABLE 8. For 7 different methods calculating $CWC(\alpha, \beta)$, for MT2010 and MT2011

10 datasets, correlation coefficients (cc) between $CWC(\alpha, \beta)$ and fitted CWC(Z) and CWC(Z,T),

11 respectively, are shown in the left column. In addition, expected value E, 1st quartile, median,

12 3rd quartile and 90th percentile of $error_Z$ and $error_{Z,T}$ are presented. Also calculated below:

13 $error_{Z,T}$ - $error_Z$.

CWC(Z) versus CWC(α, β) ; error$_Z$: E, 1/4, 1/2, 3/4, 9/10						
	cc	E	1/4	1/2	3/4	9/10
T-matrix(MT2010)	0.96	24	7	15	28	52
T-matrix (MT2011)	0.95	39	14	29	48	70
MT2010(equation17)	0.86	43	12	23	41	91
MT2011(equation18)	0.86	75	18	37	62	112
mean(MT2010)(equation19)	0.85	49	15	29	48	103
mean(MT2011)(equation20)	0.85	75	20	41	63	111
MT2010(equation21)	0.89	40	11	22	40	86
MT2011(equation22)	0.87	71	17	35	60	111
H10(NAMMA)	0.84	51	15	30	49	105
H10(cv-gt)	0.85	75	20	41	62	110
BF95(MT2010)	0.83	54	16	32	53	113
BF95(MT2011)	0.84	72	20	43	65	118
CWC(Z,T) versus CWC(α, β) ; error$_{Z,T}$: E, 1/4, 1/2, 3/4, 9/10						
	cc	E	1/4	1/2	3/4	9/10
T-matrix(MT2010)	0.90	22	7	14	25	47
T-matrix (MT2011)	0.93	34	11	24	42	66
MT2010(equation17)	0.75	40	10	21	40	84
MT2011(equation18)	0.82	71	17	35	60	106
mean(MT2010)(equation19)	0.81	39	10	22	40	83
mean(MT2011)(equation20)	0.84	66	16	34	59	102
MT2010(equation21)	0.79	38	10	21	40	83
MT2011(equation22)	0.83	69	17	35	59	106
H10(NAMMA)	0.81	38	10	21	39	79
H10(cv-gt)	0.84	66	16	34	59	102
BF95(MT2010)	0.81	38	10	21	39	76
BF95(MT2011)	0.84	63	16	35	60	104
error$_{Z,T}$ - error$_Z$						
		E	1/4	1/2	3/4	9/10
T-matrix(MT2010)		-2	0	-1	-3	-5
T-matrix (MT2011)		-5	-3	-5	-6	-4
MT2010(equation17)		-3	-1	-1	0	-7
MT2011(equation18)		-4	-1	-2	-1	-6
mean(MT2010)(equation19)		-11	-5	-7	-8	-20
mean(MT2011)(equation20)		-9	-4	-8	-3	-10
MT2010(equation21)		-1	-1	-1	0	-3
MT2011(equation22)		-2	0	-1	0	-5
H10(NAMMA)		-13	-5	-9	-11	-26
H10(cv-gt)		-9	-4	-7	-3	-9
BF95(MT2010)		-16	-6	-11	-14	-36
BF95(MT2011)		-10	-4	-9	-5	-14

1

MT 2010   MT 2011

-29°C   -29°C
-25°C   -25°C
-20°C   -20°C
-17°C   -17°C
-12°C   -12°C
-5°C   -5°C
-1°C   -1°C

1

2   FIG. 1. Examples of 2D images recorded by the precipitation imaging probe PIP for MT2010

3   and MT2011. Selected hydrometeor images are presented as a function of temperature in °C

4   and have sizes between 2mm to 4mm.
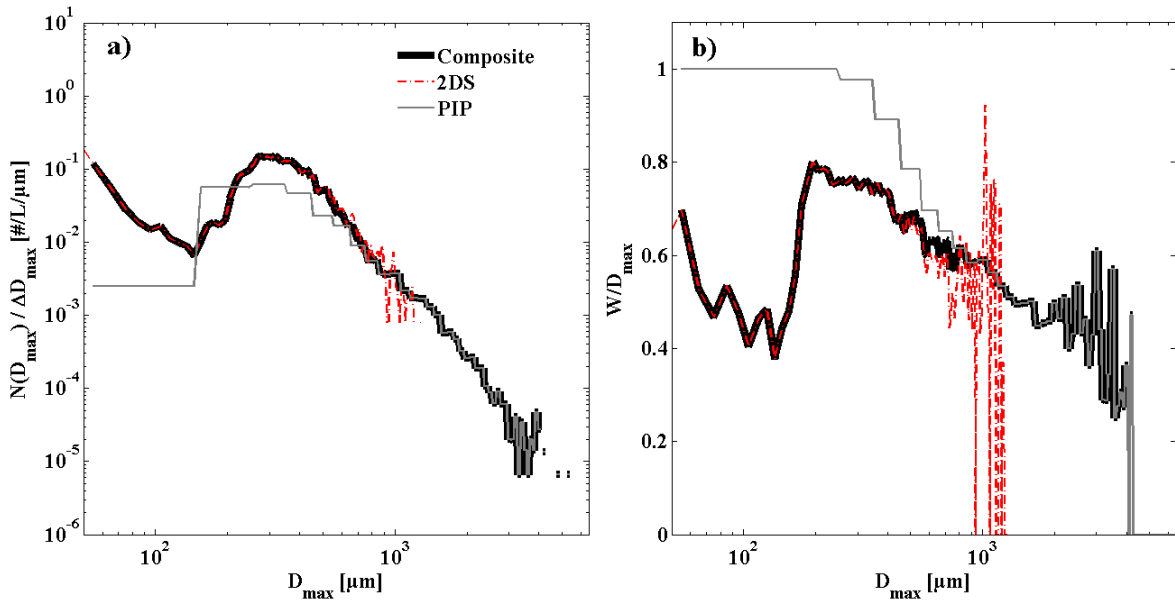
5

6   FIG. 2. a) Number size distributions (as a function of D_{max}) of cloud particles. The dashed red

7   line represents the 2D-S data, the grey line the PIP data, and the bold black line represents the

8   composite particle number size distribution (PSD). b) Aspect ratio of 2D particles as a

9   function of D_{max}. Symbols for 2D-S and PIP as above. All curves (number size distributions

10   and aspect ratios) represent an average over 5 seconds of measurements.

1

3D symbols	individual 3D shapes	Aggregates of 3D shapes	Examples of measured hydrometeors

2
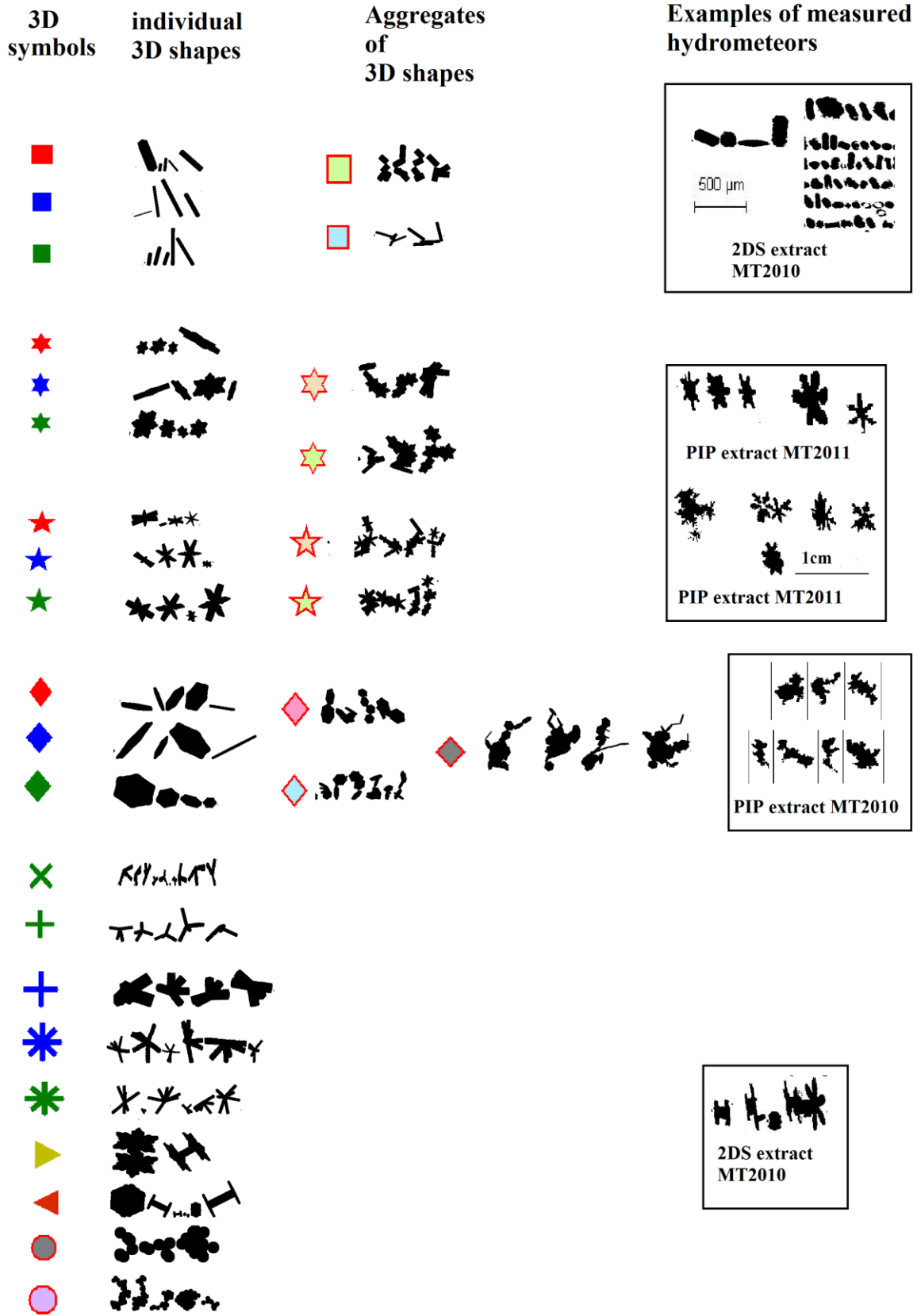
1   Fɪɢ. 3. To the left are presented examples of 2D projections of randomly oriented individual

2   3D shapes (single hydrometeors) with their corresponding symbols as they are used in

3   subsequent Fig. 4 and in Table 2. In the middle column are shown examples of aggregates

4   composed of respective single individual shapes to the left. The right column shows examples

5   of measured natural crystals resembling more or less the 3D simulations with respective

6   projections.

7
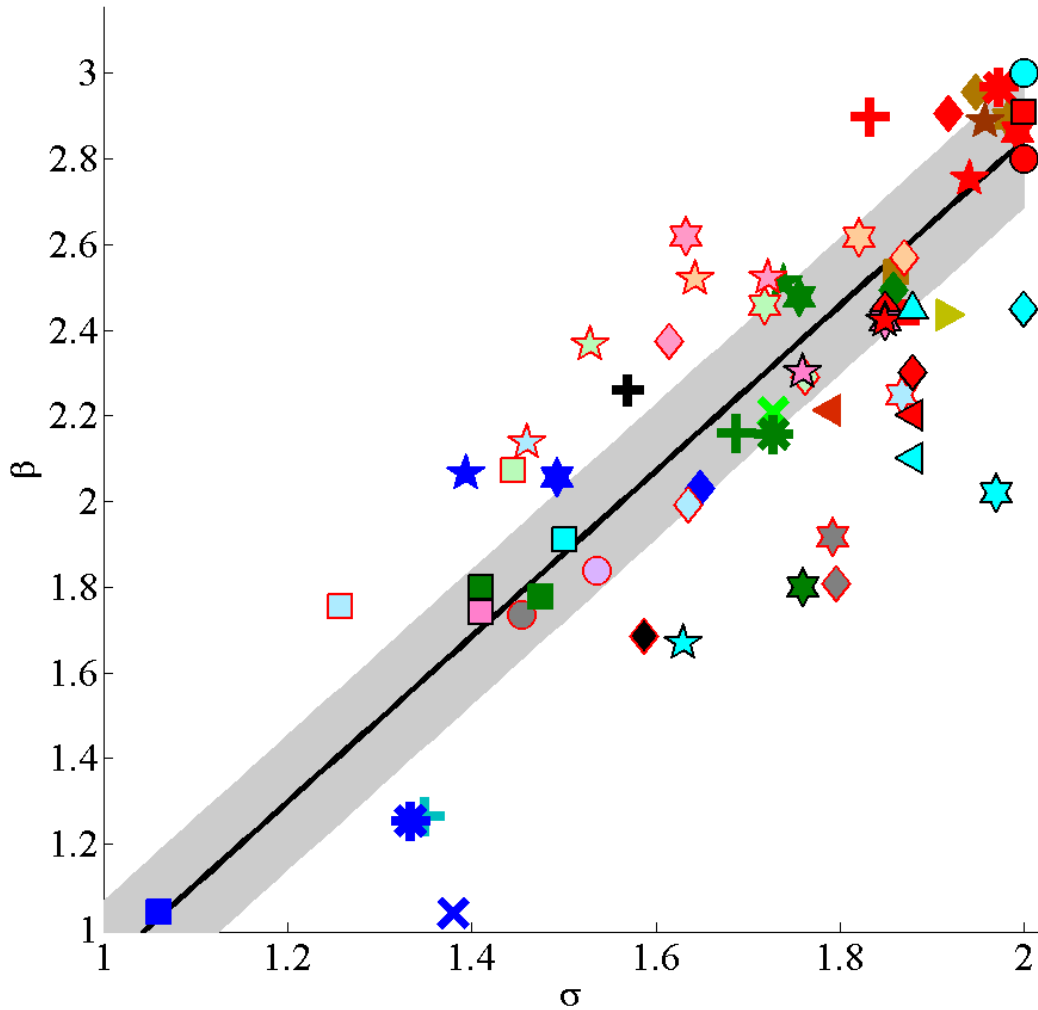
8   Fɪɢ. 4. Exponent β of m(D) relationship as a function of the exponent σ of the S(D)

9   relationship. All data point either with red contours or without contours have been deduced

10   for a population of 1000 simulated 3D shapes and corresponding projections. Symbols with

11   red contours are deduced for 3D aggregates of crystals of an elementary shape. Symbols with

12   black contours stem from M96. The legend for symbols is given in Table 2. A linear fit of all

1   simulated data is shown by the black line. The grey band represents the mean standard

2   deviation (± 0.16)

3
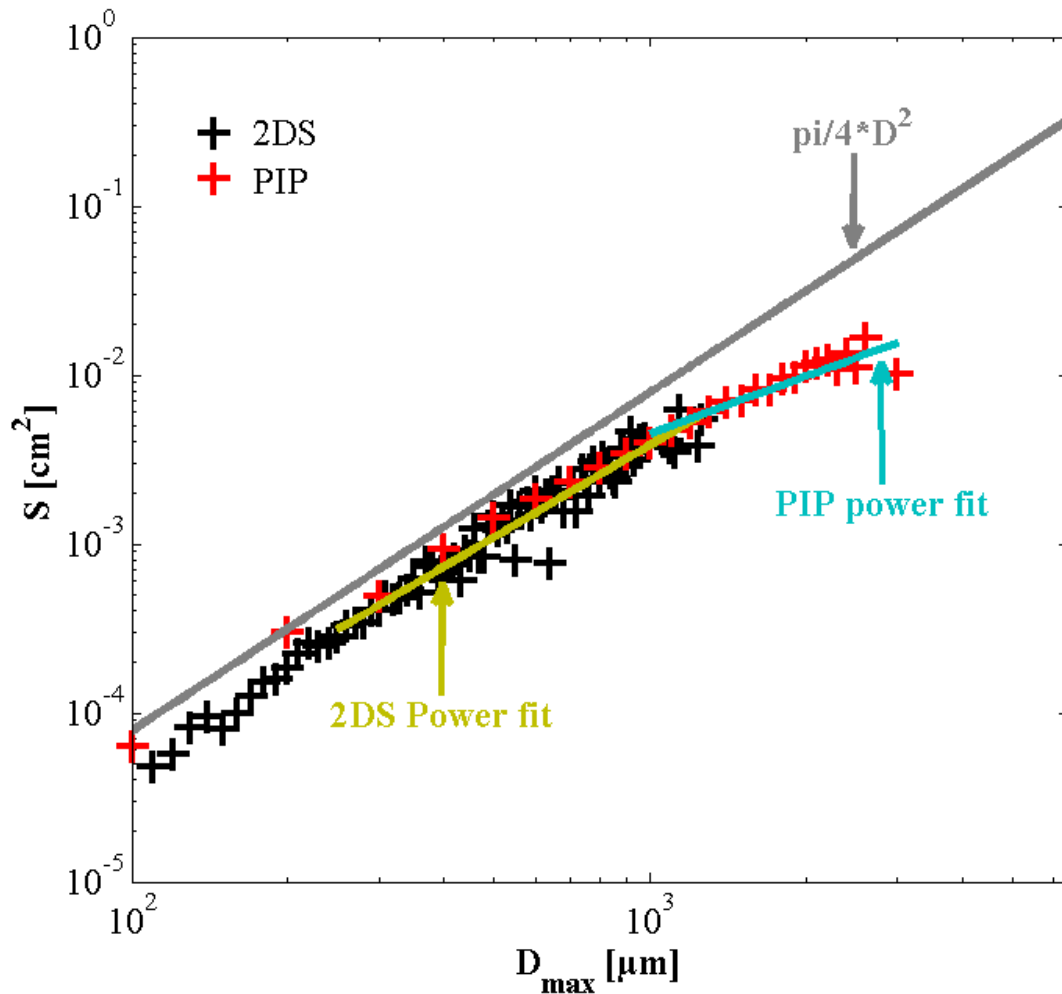
4   Fɪɢ. 5. Mean projected surface versus Dmax. Black symbols represent the 2D-S image data

5   and red symbols the PIP data. The grey line would be the power law fit for spherical particles.

6   The golden line is the power law which fits the 2D-S data for D_{max} larger than 250µm and the

7   blue line fits the PIP data with a power law for D_{max} larger than 950µm.

8

9

10
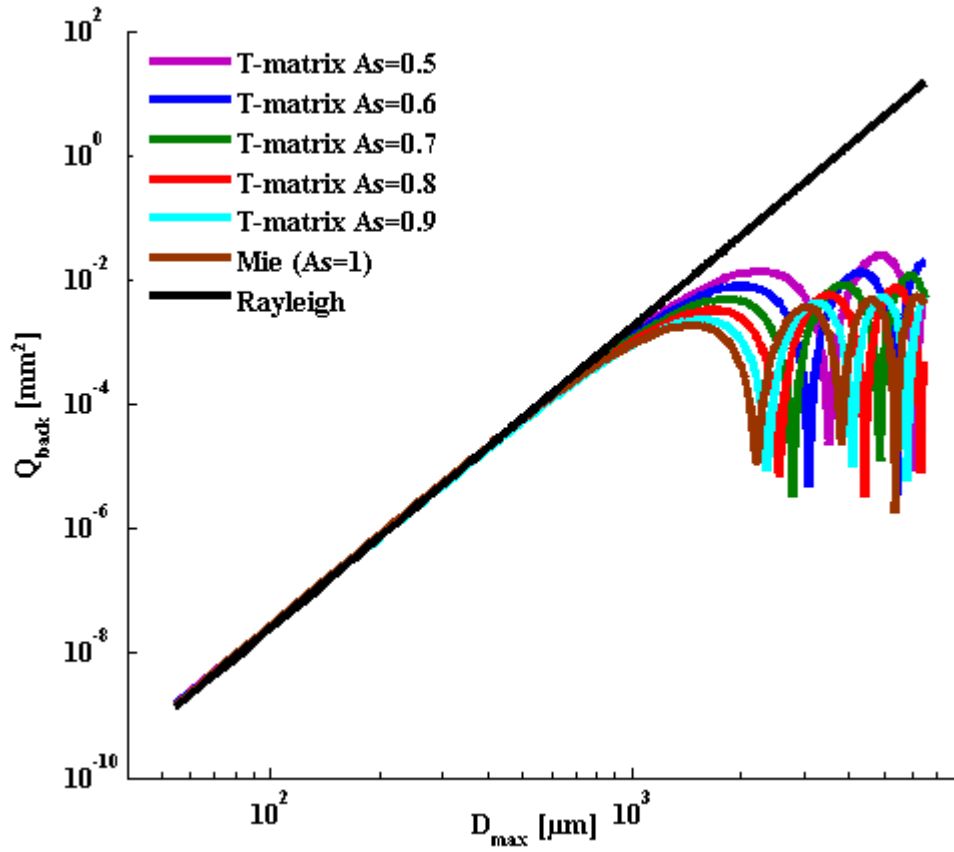
1

2 FIG. 6. Calculated backscattering cross section as a function of the maximum particle
3 diameter D_{max}. Pink, blue, green, red and cyan curves are calculated for different Aspect ratios
4 by the T-matrix method, whereas the brown curve is based on the Mie theory calculation for a
5 spherical particle. The black curve represents the Rayleigh approximation.

6
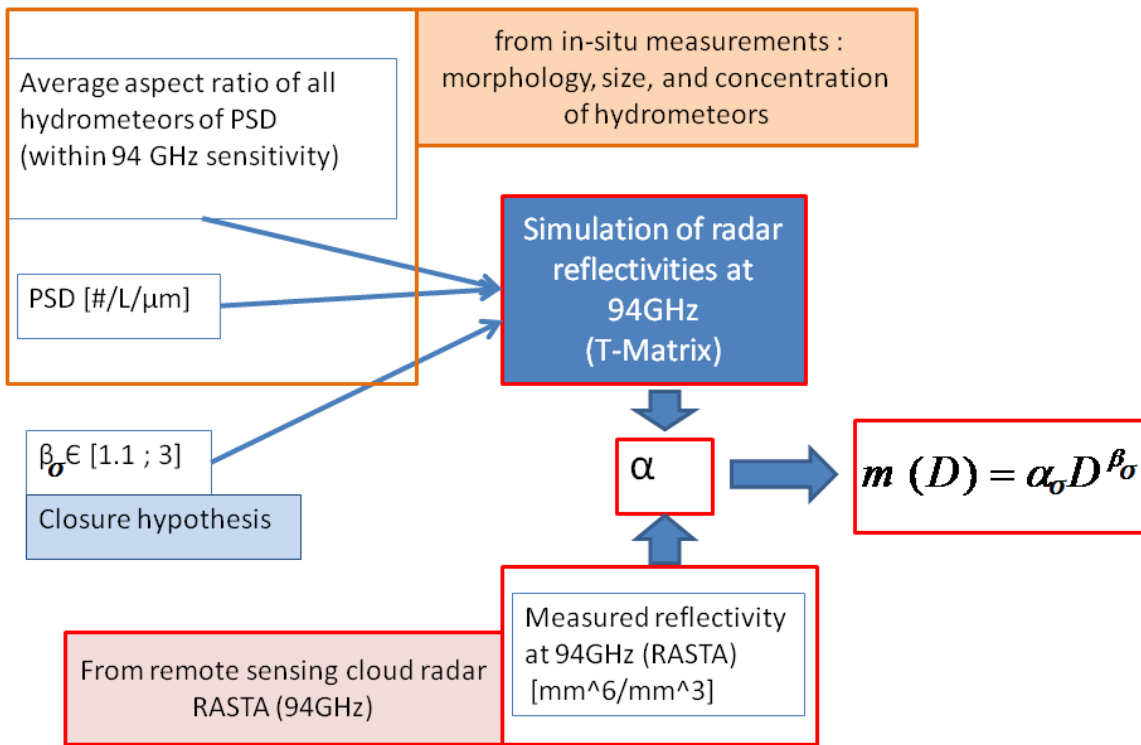
FIG. 7. Implemented method to retrieve the coefficients (pre-factor and exponent) of the mass-diameter relationship from the combination of radar reflectivity and 2D hydrometeor images. Measured radar reflectivity and hydrometeor particle size distributions and average aspect ratios serve as input for the T-matrix method used for reflectivity simulations for variable β_σ exponents. Closure hypothesis between measured and simulated reflectivities then yield the pre-factor α_σ.

1
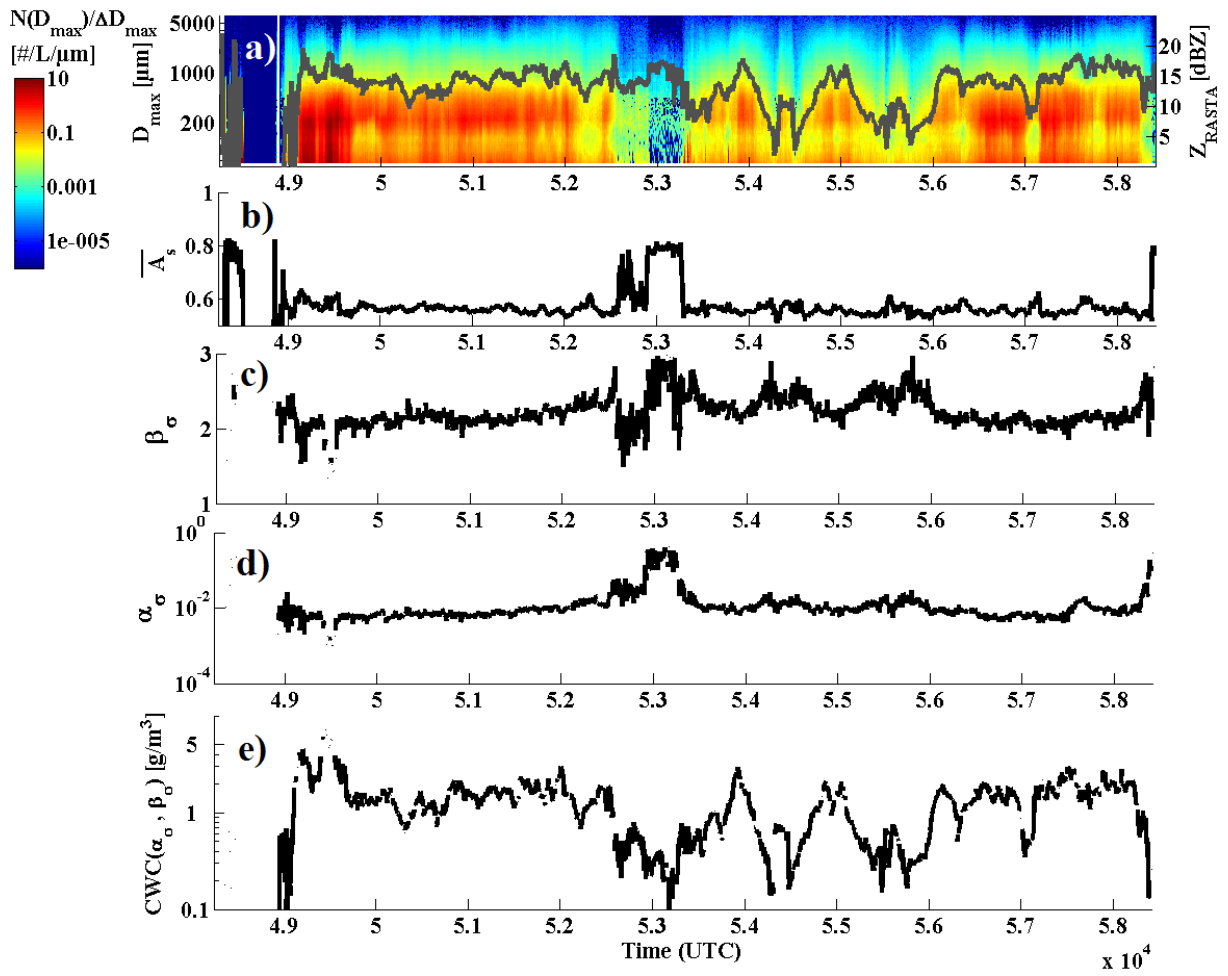
FIG. 8. (a) Contour plot of the time series of the number PSD (as a function of D_{max}) color coded with the number concentration, the grey line shows the simultaneously measured radar reflectivity (secondary y axis). (b) Mean aspect ratio along the flight. (c) β_σ exponent calculated from σ according to equations 5 and 7. (d) Pre-factor α_σ, subsequently deduced with the T-Matrix method. (e) CWC calculated with α_σ and β_σ presented above.

1
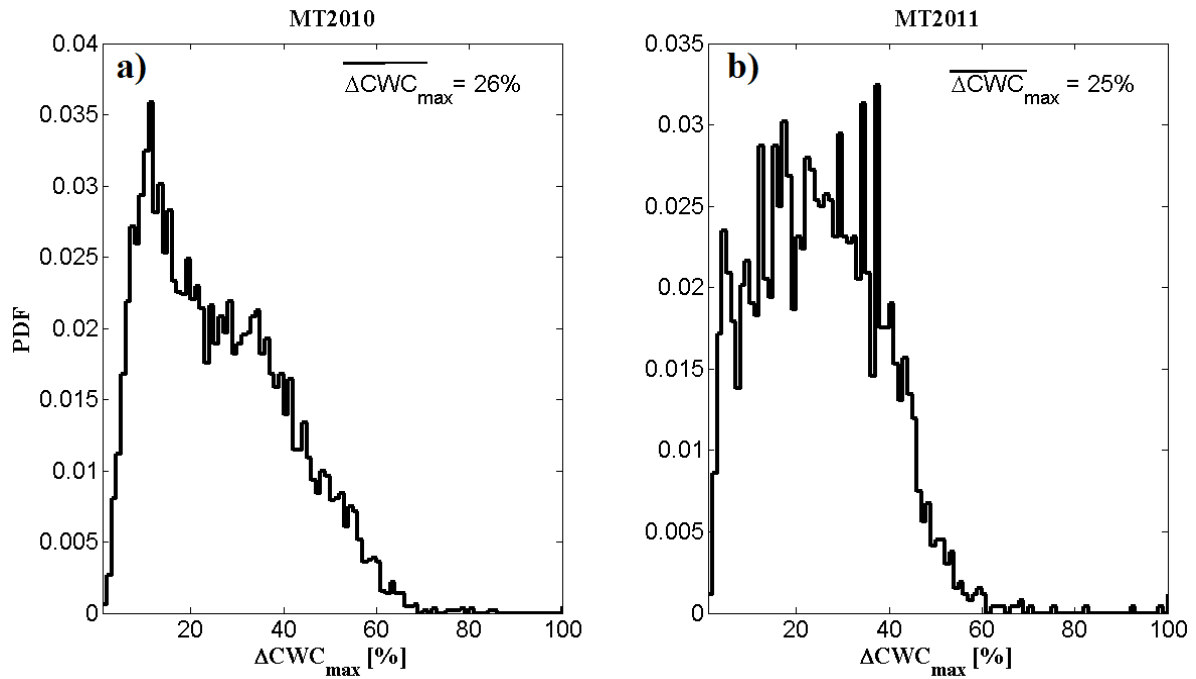
FIG. 9. Histograms of the maximum deviation (ΔCWC_{max}) on the retrieved CWC for a) MT2010 and b) MT2011.

4
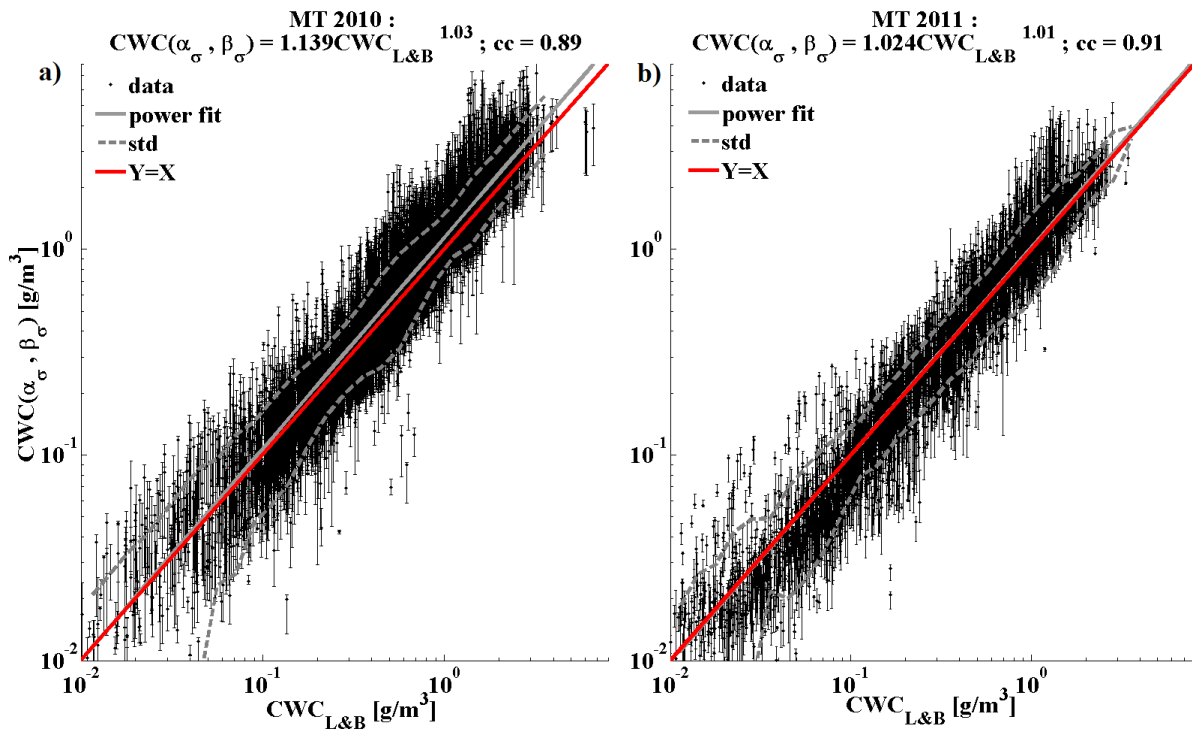
FIG. 10. $CWC(\alpha_\sigma, \beta_\sigma)$ retrieved with T-matrix method including error bars versus $CWC_{L\&B}$ calculated from Baker and Lawson (2006) for a) MT2010 and b) MT2011. Error bars represent the minimum and the maximum of all possible CWC values, when β varies between

46

1 [1; 3]. The solid grey line represents a power law fit relating the two calculations. The dashed

2 grey lines represent the standard deviation and the red line represents a 1:1 relation between

3 CWC (α_σ, β_σ) and CWC$_{L\&B}$.

4

5
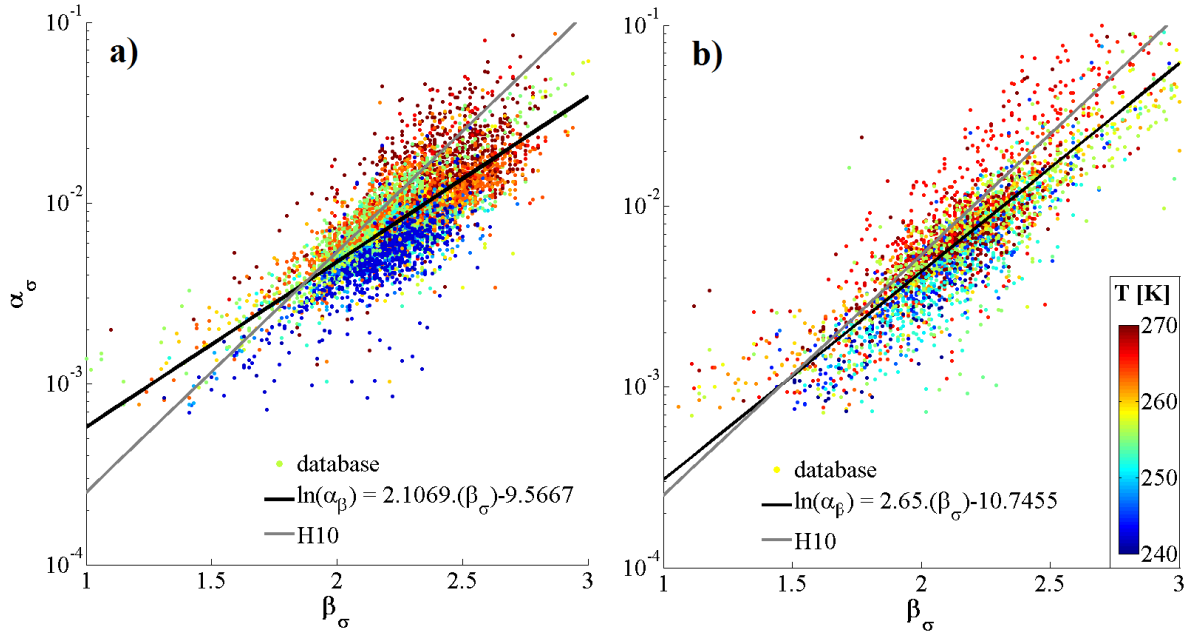
6 FIG. 11. Scatter plot of exponent β_σ as a function of α_σ. Data points are color coded as a

7 function of temperature; black lines represent power law fits. The grey lines represent added

8 m(D) power law fits for CRYSTAL-FACE data from H10. a) MT2010 and b) MT2011.

9
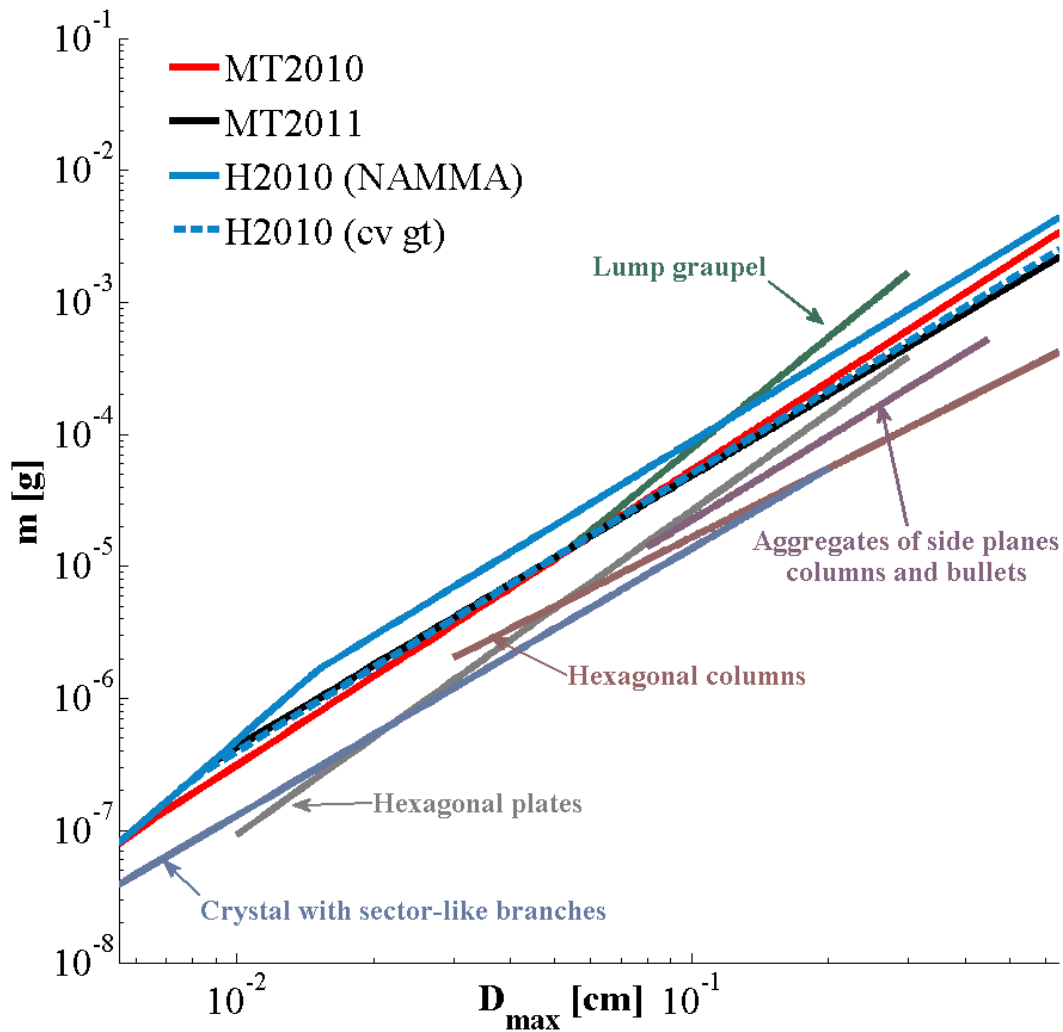
FIG. 12. Mass of individual ice crystals in gram as a function of their D_{max}.. The red line represents mean values of m(D) coefficients for MT2010 (equation 19). Likewise, the black dashed line represents m(D) coefficients for MT2011 (equation 20). The blue line represents m(D) coefficients taken from H10 for the NAMMA campaign and the dashed blue line also stems from H10, but for convectively generated. Finally, various m(D) relationships are taken from M96, as there are the blue-grey line for crystals with sector-like branches, the grey line for hexagonal plates, the brown-grey line for hexagonal columns, the purple-grey line for aggregates of side planes columns and bullets, and the green line for lump graupel.
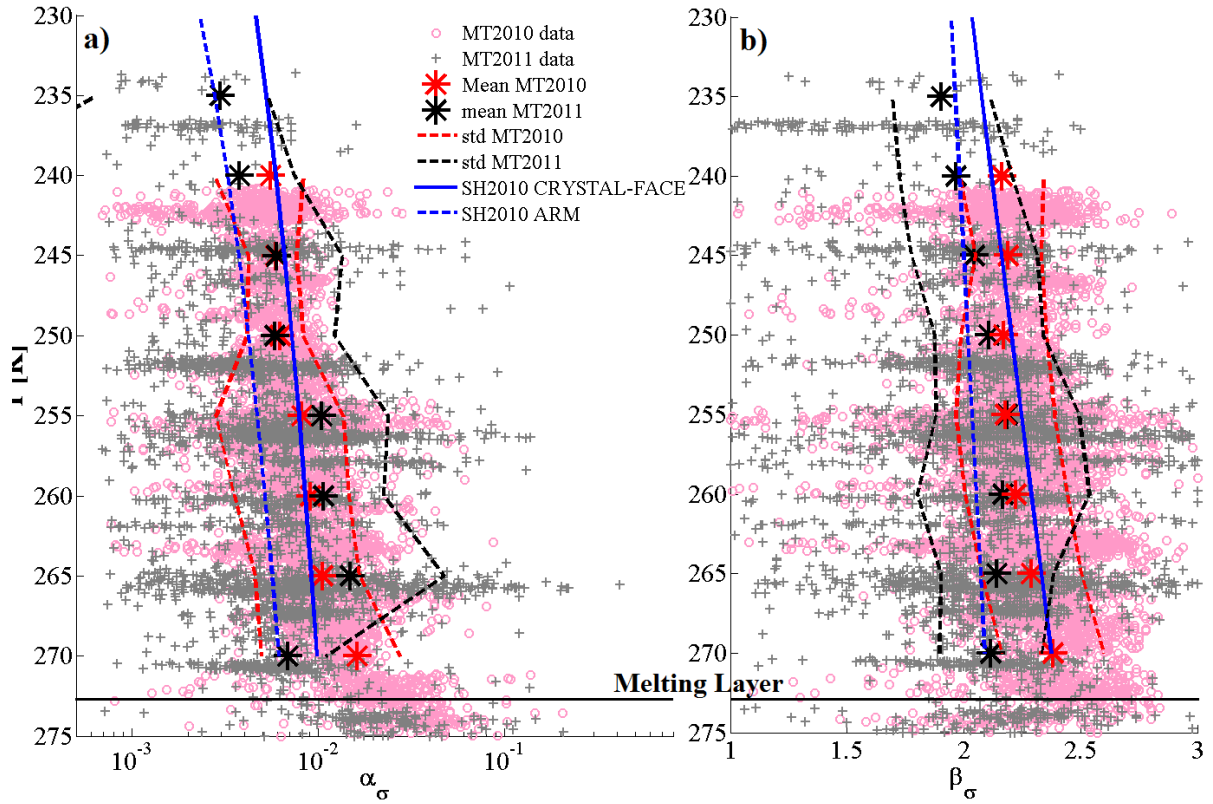
FIG. 13. Vertical variability of m(D) coefficients α_σ and β_σ. (a) α_σ versus the temperature in K. (b) β_σ versus the temperature in K. Small symbols of pink circles show data points (5-seconds time step) of MT2010, whereas grey crosses show MT2011 data. Large symbols of red and black stars present mean values of m(D) coefficients in 5K temperature intervals for MT2010 and MT2011, respectively. Dashed red and black lines show standard deviations from the mean value for MT2010 and MT2011, respectively. Blue solid and dashed lines show vertical profiles of SH2010 obtained for CRYSTAL-FACE and for ARM campaigns, respectively.
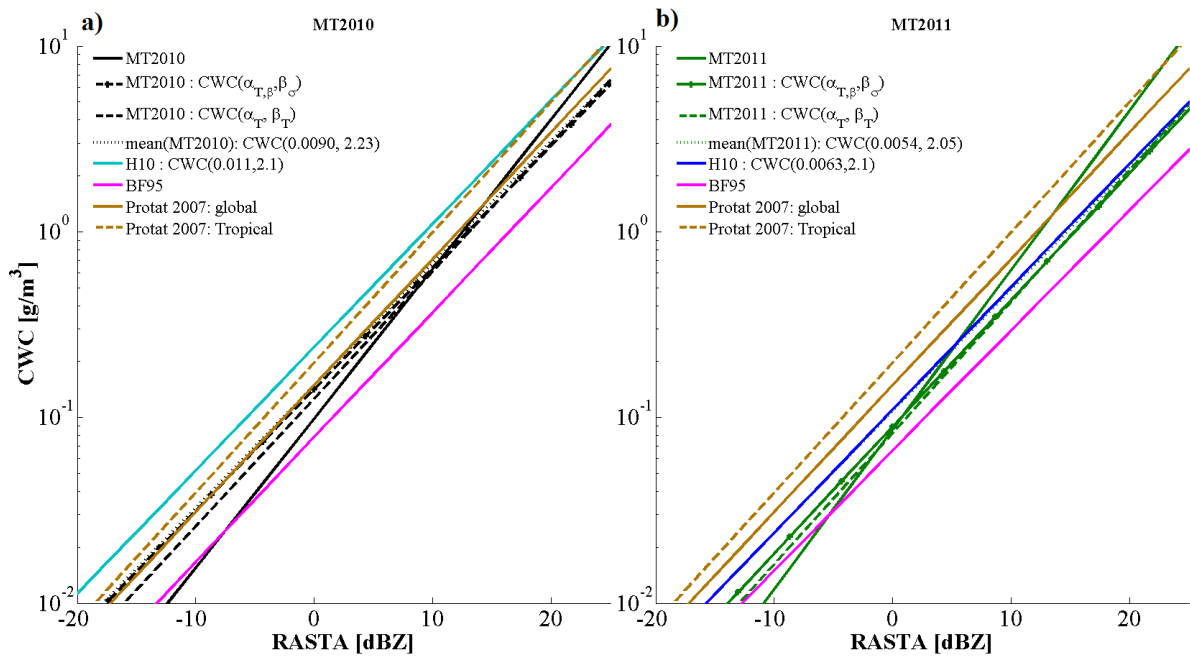
FIG. 14. Z-CWC fitted relationships between calculated CWC and measured radar reflectivies for MT2010 and MT2011 datasets. Z is given in dBZ on the x axis and CWC in g m^{-3} on the y axis. a) Power law fits for MT2010. b) Power law fits for MT2011.
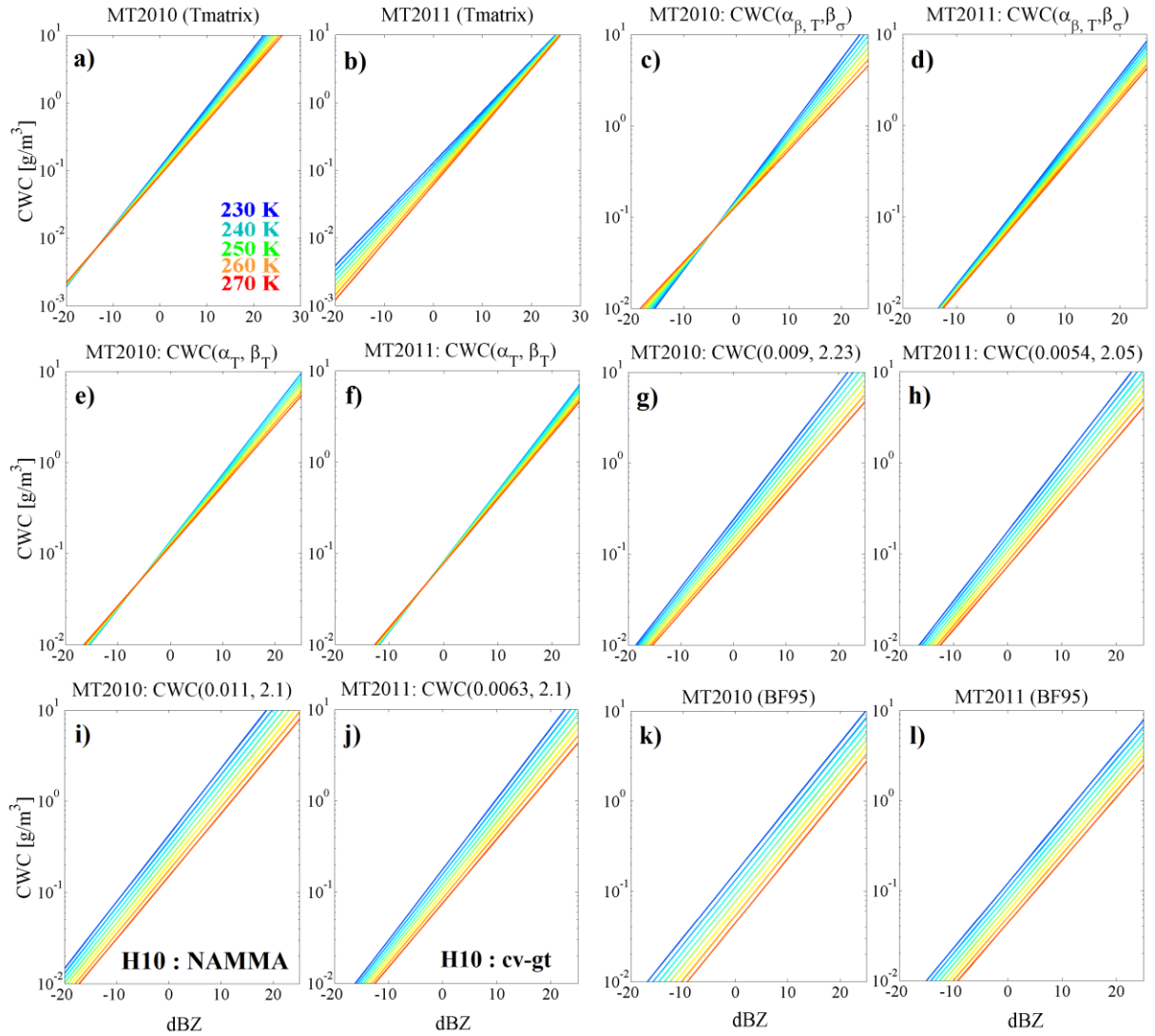
FIG. 15. Z-CWC-T fitted relationships between calculated CWC and measured radar reflectivies and temperatures for MT2010 and MT2011 datasets. Z is given in dBZ on the x axis and CWC in g m^{-3} on the y axis. a) CWC are calculated from α_σ and β_σ for MT2010 dataset. b) as for a) but for MT2011. c) CWC are calculated using $\alpha_{\beta,T}$ and β_σ for MT2010 dataset. d) as for c) but for MT2011. e) CWC are calculated as a function of α_T and β_T for MT2010 (equation 21). f) as for e) but for MT2011 (equation 22). g) CWC are calculated from average coefficient of MT2010 (equation 19). h) as for g) but for MT2011 (equation 20). i) CWC are calculated using H10 m(D) coefficients of NAMMA for MT2010. j) CWC are calculated using H10 m(D) coefficients of clouds convectively generated for MT2011. k) CWC are calculated using the BF95 parametrisation for MT2010 dataset. l) as for k) but for MT2011.
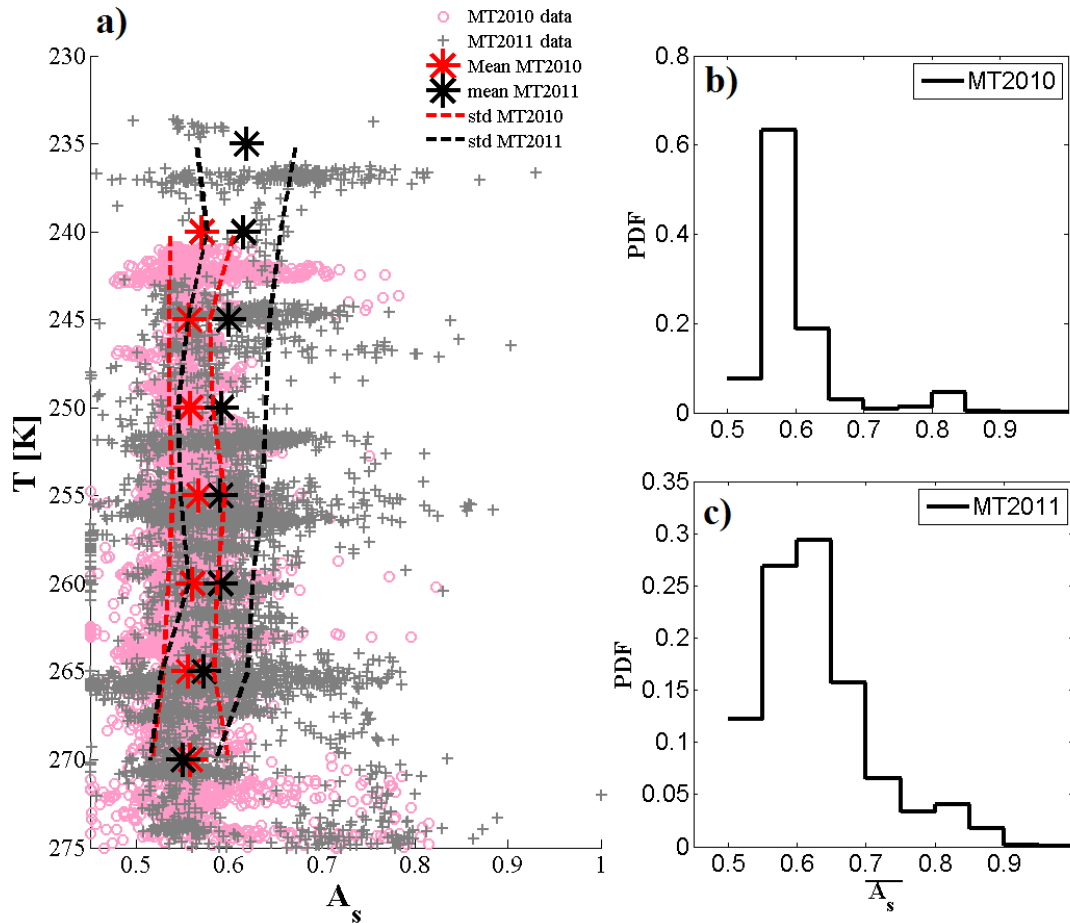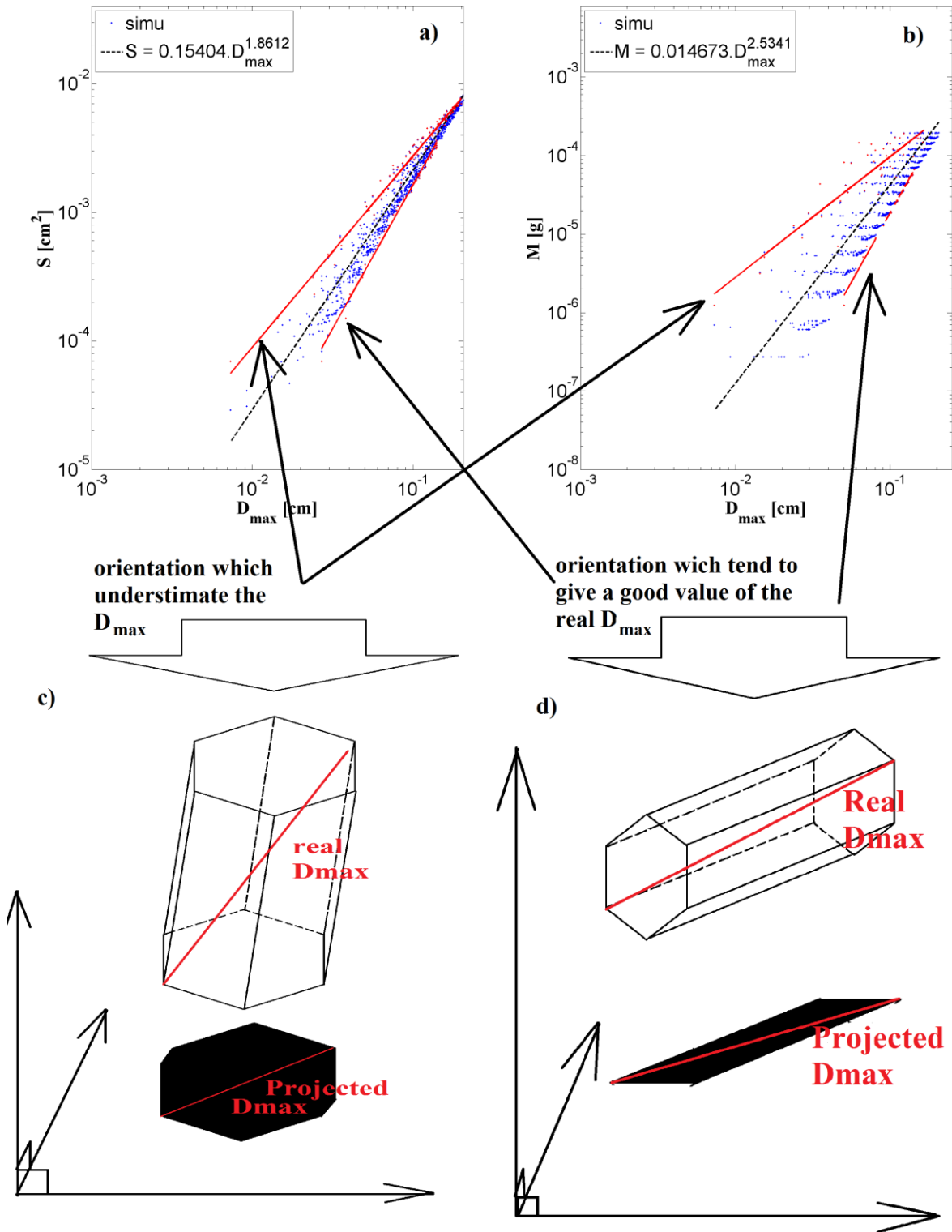
FIG. 16. a) Vertical profiles of the average aspect ratio $\overline{As}$ as a function of temperature. Small symbols of pink circles show data points (5-seconds time step) of MT2010, whereas grey crosses show MT2011 data. Large symbols of red and black stars present mean values of $\overline{As}$ in 5K temperature intervals for MT2010 and MT2011, respectively. Dashed red and black lines show standard deviations for MT2010 and MT2011, respectively, from the average value. b) Probability distribution functions of $\overline{As}$ for MT2010. c) Probability distribution functions of $\overline{As}$ for MT2011.

**Simulations of Hexagonal Columns such L=0.2*H**

a) legend:
- simu
- $S = 0.15404 \cdot D_{max}^{1.8612}$

S [cm^2], D_{max} [cm]

b) legend:
- simu
- $M = 0.014673 \cdot D_{max}^{2.5341}$

M [g], D_{max} [cm]

orientation which understimate the D_{max}

orientation wich tend to give a good value of the real D_{max}

c) real Dmax, Projected Dmax

d) Real Dmax, Projected Dmax

1

2 FIG. A1. Exemplary results obtained for a 3D simulation of columns characterized by

3 length=0.2*height. a) S(D) plot: Blue points are the simulated data for the column, red lines

4 are power law fits enclosing most of the data points for all possible orientations. The dashed

1 black line is the mean of the two power laws (= the mean between two red lines when the

2 orientation underestimates Dmax and when the orientation is close to the real D_{max}). b) m(D)

3 plot: same as for a) but with the mass of the simulated columns which is now on the y-axis; c)

4 Schematic of a 3D shape oriented in the 3D space when its orientation gives an

5 underestimated value of the real D_{max} of the ice crystals. d) Schematic of a 3D shape oriented

6 in the 3D space when its orientation gives a close value of the real D_{max} of the ice crystals.
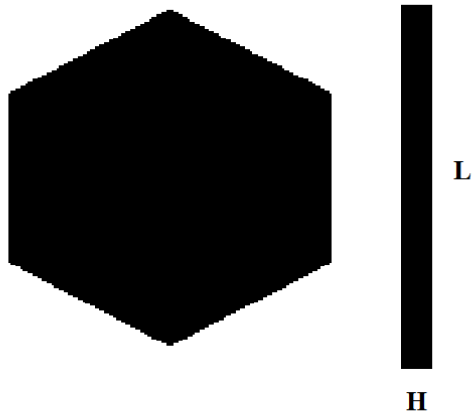
7

8 FIG. A2. Schematic description of hydrometeors shapes for subsequent simulations of plates.
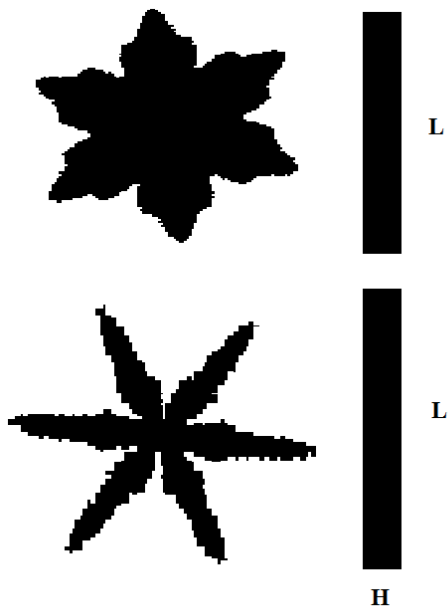
9
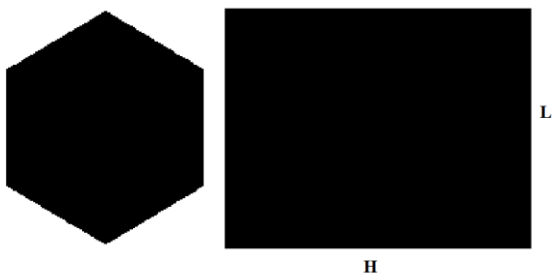
10

11 FIG. A3. Schematic description of hydrometeors shapes for subsequent simulations of
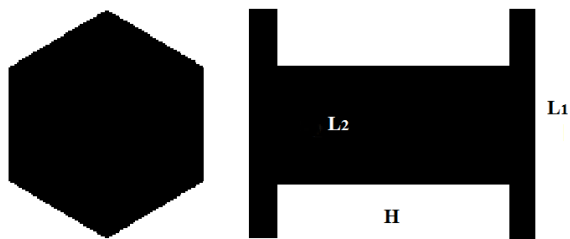
12 columns.

13

1

2 FIG. A4. Schematic description of hydrometeors shapes for subsequent simulations of slender
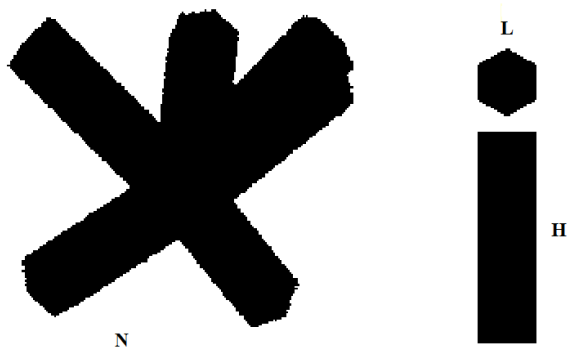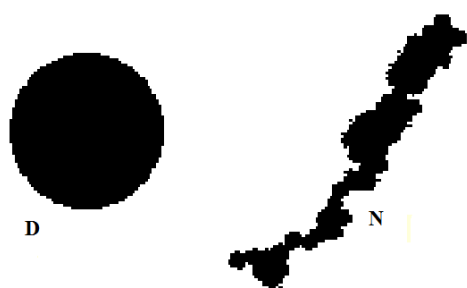
3 and solid stellars.

4

5

6

7 FIG. A5. Schematic description of hydrometeors shapes for subsequent simulations of capped

8 columns.

9

1

2 FIG. A6. Schematic description of hydrometeors shapes for subsequent simulations of bullet

3 rosettes.

4

5 FIG. A7. Schematic description of hydrometeors shapes for subsequent simulations of

6 aggregates of spheres.

7